

# The WiggleZ Dark Energy Survey: Survey Design and First Data Release

Michael J. Drinkwater<sup>1\*</sup>, Russell J. Jurek<sup>1</sup>, Chris Blake<sup>2</sup>, David Woods<sup>3,4</sup>, Kevin A. Pimblet<sup>1</sup>, Karl Glazebrook<sup>2</sup>, Rob Sharp<sup>5</sup>, Michael B. Pracy<sup>2,6</sup>, Sarah Brough<sup>2</sup>, Matthew Colless<sup>5</sup>, Warrick J. Couch<sup>2</sup>, Scott M. Croom<sup>7</sup>, Tamara M. Davis<sup>1,8</sup>, Duncan Forbes<sup>2</sup>, Karl Forster<sup>9</sup>, David G. Gilbank<sup>10</sup>, Michael Gladders<sup>11</sup>, Ben Jelliffe<sup>7</sup>, Nick Jones<sup>2</sup>, I-hui Li<sup>2</sup>, Barry Madore<sup>12</sup>, D. Christopher Martin<sup>9</sup>, Gregory B. Poole<sup>2</sup>, Todd Small<sup>9</sup>, Emily Wisnioski<sup>2</sup>, Ted Wyder<sup>9</sup>, H.K.C. Yee<sup>13</sup>

<sup>1</sup>Department of Physics, The University of Queensland, Brisbane, QLD 4072, Australia

<sup>2</sup>Centre for Astrophysics & Supercomputing, Swinburne University of Technology, P.O. Box 218, Hawthorn, VIC 3122, Australia

<sup>3</sup>Department of Physics & Astronomy, University of British Columbia, 6224 Agricultural Road, Vancouver, B.C., V6T 1Z1, Canada

<sup>4</sup>School of Physics, University of New South Wales, Sydney, NSW 2052, Australia

<sup>5</sup>Anglo-Australian Observatory, P.O. Box 296, Epping, NSW 2121, Australia

<sup>6</sup>Research School of Astronomy & Astrophysics, Australian National University, Weston Creek, ACT 2600, Australia

<sup>7</sup>Sydney Institute for Astronomy, School of Physics, University of Sydney, NSW 2006, Australia

<sup>8</sup>Dark Cosmology Centre, Niels Bohr Institute, University of Copenhagen, DK-2100 Copenhagen, Denmark

<sup>9</sup>California Institute of Technology, MC 405-47, 1200 East California Boulevard, Pasadena, CA 91125, United States

<sup>10</sup>Department of Physics and Astronomy, University Of Waterloo, Waterloo, Ontario N2L 3G1, Canada

<sup>11</sup>Department of Astronomy and Astrophysics, The University of Chicago, 5640 S. Ellis Ave., Chicago, IL 60637, United States of America

<sup>12</sup>Observatories of the Carnegie Institute of Washington, 813 Santa Barbara St., Pasadena, CA 91101, United States of America

<sup>13</sup>Department of Astronomy & Astrophysics, University of Toronto, 50 St. George St., Toronto, ON, M5S 3H4, Canada

Accepted 2009 September 21

## ABSTRACT

The WiggleZ Dark Energy Survey is a survey of 240,000 emission line galaxies in the distant universe, measured with the AAOmega spectrograph on the 3.9-m Anglo-Australian Telescope (AAT). The primary aim of the survey is to precisely measure the scale of baryon acoustic oscillations (BAO) imprinted on the spatial distribution of these galaxies at look-back times of 4–8 Gyrs.

The target galaxies are selected using ultraviolet photometry from the GALEX satellite, with a flux limit of  $NUV < 22.8$  mag. We also require that the targets are detected at optical wavelengths, specifically in the range  $20.0 < r < 22.5$  mag. We use the Lyman break method applied to the ultraviolet colours, with additional optical colour limits, to select high-redshift galaxies. The galaxies generally have strong emission lines, permitting reliable redshift measurements in relatively short exposure times on the AAT. The median redshift of the galaxies is  $z_{med} = 0.6$ . The redshift range containing 90% of the galaxies is  $0.2 < z < 1.0$ .

The survey will sample a volume of  $\sim 1 \text{ Gpc}^3$  over a projected area on the sky of  $1,000 \text{ degree}^2$ , with an average target density of  $350 \text{ degree}^{-2}$ . Detailed forecasts indicate the survey will measure the BAO scale to better than 2% and the tangential and radial acoustic wave scales to approximately 3% and 5%, respectively. Combining the WiggleZ constraints with existing cosmic microwave background measurements and the latest supernova data, the marginalized uncertainties in the cosmological model are expected to be  $\sigma(\Omega_m) = 0.02$  and  $\sigma(w) = 0.07$  (for a constant  $w$  model). The WiggleZ measurement of  $w$  will constitute a robust, precise and independent test of dark energy models.

This paper provides a detailed description of the survey and its design, as well as the spectroscopic observations, data reduction, and redshift measurement techniques employed. It also presents an analysis of the properties of the target galaxies, including emission line diagnostics which show that they are mostly extreme starburst galaxies, and *Hubble Space Telescope* images, which show they contain a high fraction of interacting or distorted systems. In conjunction with this paper, we make a public data release of data for the first 100,000 galaxies measured for the project.

**Key words:** surveys – galaxies: high-redshift – galaxies: photometry – galaxies: starburst – cosmology: observations – ultraviolet: galaxies

## 1 INTRODUCTION

A major theme of cosmology for several decades has been the determination of the best cosmological model to describe our Universe. By the early 1990s, evidence was already accumulating from measurements of large-scale structure and the cosmic microwave background that if the Universe was flat, the matter density was well below the critical value, requiring an additional (large) contribution from a non-zero cosmological constant term (Efstathiou, Sutherland, & Maddox 1990). This “ $\Lambda$ CDM” cosmology, dominated by the cosmological constant ( $\Lambda$ ) and cold dark matter (CDM), although radical at the time, predicted an older age for the Universe than other models, so was more consistent with observational lower limits to the age (Ostriker & Steinhardt 1995). Additional early support for a non-zero cosmological constant was provided by Yoshii & Peterson (1991, 1995) in their analysis of faint near-infrared galaxy counts. The case for a  $\Lambda$ CDM cosmology was strengthened dramatically in the late 1990s by the measurement from distant type Ia supernovae of the acceleration in the expansion rate of the Universe (Riess et al. 1998; Perlmutter et al. 1999).

The goal of cosmology now is to test different models of the underlying physics responsible for this acceleration, dubbed “dark energy”. This research has focused around the dark energy equation of state (parameterised by  $w(z)$ , so pressure equals  $w$  times density) and how it changes with time. A central goal is to measure  $w(z)$  at multiple redshifts to test various dark energy models (Frieman et al. 2008). A powerful way to test the dark energy models is to measure the geometrical relations between distance and redshift. These can be measured by observing the baryon acoustic oscillation (BAO) scale imprinted on the distribution of baryonic matter at recombination (Cooray et al. 2001; Eisenstein 2002; Blake & Glazebrook 2003; Seo & Eisenstein 2003; Hu & Haiman 2003; Linder 2003; Glazebrook & Blake 2005). The BAO signal has been clearly measured in the cosmic microwave background (i.e. at recombination; Bennett et al. 2003). More recently, the 2dF Galaxy Redshift Survey; (2dFGRS, Colless et al. 2001) and the Sloan Digital Sky Survey (SDSS, York et al. 2000) have permitted the detection of the BAO signal in the distribution of low-redshift ( $z \approx 0.2$ – $0.35$ ) galaxies. The 2dFGRS detection was reported by Cole et al. (2005) and Percival et al. (2007); the SDSS result was reported by Eisenstein et al. (2005), Hütsi (2006) and Percival et al. (2007). These galaxy samples are too nearby to be sensitive to the cosmic effects of dark energy, but provide a superb validation of the concept.

Measurement of the BAO scale in the galaxy distribution at high redshifts provides a powerful test of the dark energy models. It gives a geometrical measurement of the Universe at different redshifts which delineates the cosmic expansion history with high accuracy and traces the effects of dark energy (Blake & Glazebrook 2003). It also provides a unique and direct measurement of the expansion rate at high redshift (Glazebrook & Blake 2005). The most important advantage of the BAO measurement is that its measurement is completely independent of the supernova results and, in particular, is less susceptible to systematic errors. It is also complementary to the supernova results in that the

measurement uncertainties are orthogonal to those of the supernova measurements (Blake et al. 2009a).

The WiggleZ Dark Energy Survey is a major large-scale structure survey of UV-selected emission-line galaxies. The survey is designed to map a cosmic volume large enough to measure the imprint of baryon oscillations in the clustering pattern (this requires  $\sim 1 \text{ Gpc}^3$ ; Blake & Glazebrook 2003) at a significantly higher redshift ( $0.2 < z < 1.0$ ) than has been previously achieved. Its core science goals are:

(i) To calculate the power spectrum of the galaxy distribution with sufficient precision to identify and measure the baryon acoustic oscillation scale to within 2 per cent;

(ii) To determine the value of the dark energy equation of state parameter,  $w$ , to within 10 per cent when combined with CMB data, and hence either independently validate or refute the currently-favoured “cosmological constant” model.

The redshift range of the WiggleZ Dark Energy Survey will make it the first BAO survey to sample the epoch when the universe makes the transition from matter-dominated to lambda-dominated expansion.

In this paper we present a detailed description of the survey and the key innovations that were developed to allow it to proceed. We start with a description of the survey design and its requirements in Section 2. This is followed in Section 3 with details of the selection of our target galaxies from UV data combined with optical data. The UV selection of the target galaxies means they have strong emission lines, so their redshifts can be measured in relatively short exposures on a 4m-class telescope like the Anglo-Australian Telescope (AAT). In Section 4 we describe our AAT spectroscopic observations and data reduction. The processing of our data to obtain reliable spectroscopic redshifts is detailed in Section 5. This includes analysis of the reliability of our redshifts. In Section 6, we present a summary of the initial results of the survey, notably the galaxy properties and the success of the survey design. Following this, in Section 7 we describe the data products of the survey, as released in our first public data release accompanying this paper. We summarise this paper and outline the remaining stages of the survey in Section 8.

A standard cosmology of  $\Omega_m = 0.3$ ,  $\Omega_\Lambda = 0.7$ ,  $h = 0.7$  is adopted throughout this paper.

## 2 THE SURVEY DESIGN

### 2.1 Scientific goal

The WiggleZ Dark Energy Survey is a major large-scale structure survey of intermediate-redshift UV-selected emission-line galaxies, focusing on the redshift range  $0.2 < z < 1.0$ . The survey is designed to map a cosmic volume of about  $1 \text{ Gpc}^3$ , sufficient to measure the imprint of baryon oscillations in the clustering pattern at a significantly higher redshift than has been previously achieved. The resulting measurements of cosmic distances and expansion rates, with uncertainties for each below 5%, will constitute a robust test of the predictions of the “cosmological constant” model of dark energy. Detailed forecasts for the survey are presented in Blake et al. (2009a).

## 2.2 Choice of target galaxies

The cosmological measurements from a large-scale structure survey should be independent of the galaxy type used, given that the “bias” with which galaxies trace the underlying dark matter fluctuations is expected to be a simple linear function on large scales (Coles 1993; Scherrer & Weinberg 1998). In this sense, the choice of the “tracer population” of galaxies can be determined by observational considerations such as telescope exposure times and the availability of input imaging data for target selection.

The WiggleZ Survey targets UV-selected bright star-forming galaxies, obtaining redshifts from the characteristic patterns of emission lines. A series of colour cuts, described below, are used to boost the fraction of targets lying at high redshift. The choice of blue galaxies was motivated by several considerations: (1) emission-line redshifts are generally obtainable in short 1-hour exposures at the AAT, even in poor weather, with no requirement to detect the galaxy continuum light; (2) the increasing star-formation rate density of the Universe with redshift results in a significant population of high-redshift  $z > 0.5$  targets; (3) a large fraction of UV imaging data for target selection was already available as part of the Medium Imaging Survey conducted by the Galaxy Evolution Explorer satellite (GALEX; Martin et al. 2005); (4) other large-scale structure surveys such as the Sloan Digital Sky Survey (SDSS) and the forthcoming Baryon Oscillation Spectroscopic Survey (BOSS; Schlegel, White, & Eisenstein 2009) have preferred to observe Luminous Red Galaxies, allowing the WiggleZ Survey to constrain any systematic effects arising from the choice of tracer galaxy population; and (5) interesting secondary science is achievable from studying bright star-forming galaxies at high redshift.

The main disadvantage in the choice of WiggleZ Survey targets is that emission-line galaxies possess a significantly lower clustering amplitude than red galaxies, and hence larger galaxy number densities are required to minimize the shot noise error in the clustering measurement. However, there is a benefit to the fact that WiggleZ galaxies avoid the densest environments: non-linear growth of structure—which erases linear-regime signatures in the power spectrum such as baryon oscillations—becomes less significant in the sample.

## 2.3 Target numbers

The WiggleZ Survey goal is to cover  $1,000 \text{ deg}^2$  of the equatorial sky in order to map a sufficiently large cosmic volume to measure the imprint of baryon oscillations in the clustering power spectrum. The survey was designed such that the average galaxy number density  $n_g$  is related to the amplitude of the galaxy clustering power spectrum  $P_g$  on the relevant baryon oscillation scales by  $n_g \sim 1/P_g$ , implying that the contributions of sample variance and shot noise to the clustering error are equal. This is the optimal survey strategy for a fixed number of galaxies (i.e. fixed observing time).

The galaxy selection cuts described below result in an average target density of  $340 \text{ deg}^{-2}$ . The overall survey redshift completeness, allowing for repeat observations of objects originally observed in the poorest conditions, is 70%.

The survey goal is hence to measure  $\sim 340,000$  galaxies over  $1,000 \text{ deg}^2$ , of which  $\sim 240,000$  are expected to yield successful redshifts.

We focus on the redshift range  $0.2 < z < 1.0$  which we anticipate will yield our main baryon oscillation distance measurement. The fraction of redshifts lying in this range is 90 per cent, therefore the average galaxy number density in the range  $0.2 < z < 1.0$  is  $n_g = 2.0 \times 10^{-4} h^3 \text{ Mpc}^{-3}$ . The matter power spectrum amplitude  $P_m$  at the characteristic scale of baryon oscillations ( $k = 0.15h \text{ Mpc}^{-1}$ ) is  $3800h^{-3} \text{ Mpc}^3$  at  $z = 0$  (for  $\sigma_8 = 0.9$ ). Assuming a galaxy bias of  $b = 1.21$  (Blake et al. 2009a) and a growth factor  $D = 0.74$  (at  $z = 0.6$ ), the galaxy power spectrum amplitude at  $z = 0.6$  is  $P_g = P_m D^2 b^2 = 3050h^{-3} \text{ Mpc}^3$ . Converting to redshift-space (using the boost factor  $1 + \frac{2}{3}\beta + \frac{1}{5}\beta^2$  where  $\beta = 0.5$ ) we obtain  $P_g = 4210h^{-3} \text{ Mpc}^3$ . The survey value of  $n_g \times P_g$  is therefore equal to 0.84, close to the optimal condition of  $n_g P_g = 1$ .

The average redshift completeness of an individual observation (or “pointing”) is 60% (we reach the value of 70% per galaxy mentioned above after repeating measurements made in poor conditions). Thus the total number of individual spectra required is  $N = 240,000/0.6 = 400,000$ . On average we can use 325 fibres per pointing and obtain 7.4 pointings per night, and therefore can measure the required 400,000 spectra in 166 nights of clear weather. This calculation is summarized in Table 1.

## 2.4 Survey fields

A final constraint on the survey design is the availability of suitable optical imaging catalogues in regions of sky overlapping the GALEX UV data. We require the optical data to provide more accurate positions for fibre spectroscopy and to refine our target selection. The optical data we use are from the fourth data release of the Sloan Digital Sky Survey (SDSS, Adelman-McCarthy et al. 2006) in the NGP region and from the Canada-France-Hawaii Telescope (CFHT) Second Red-sequence Cluster Survey (RCS2, Yee et al. 2007) in the SGP region.

The WiggleZ survey area, illustrated in Figure 1, is split into seven equatorial regions that sum to an area of  $1000 \text{ deg}^2$ , to facilitate year-round observing. We require that each region should possess a minimum angular dimension of  $\sim 10 \text{ deg}$ , corresponding to a spatial co-moving scale that exceeds by at least a factor of two the standard ruler preferred scale [which projects to (8.5, 4.6, 3.2, 2.6) deg at  $z = (0.25, 0.5, 0.75, 1.0)$ ]. The boundaries of the regions are listed in Table 2. We have also defined high-priority sub-regions in each area (see Table 3) which will be observed first to ensure that we have the maximum contiguous area surveyed should we be unable to observe the complete sample.

## 3 TARGET GALAXY SAMPLE

In this section we describe how we select our target galaxies from the GALEX ultraviolet data combined with additional optical imaging data. We stress that the target selection is motivated by our main science objective of measuring the

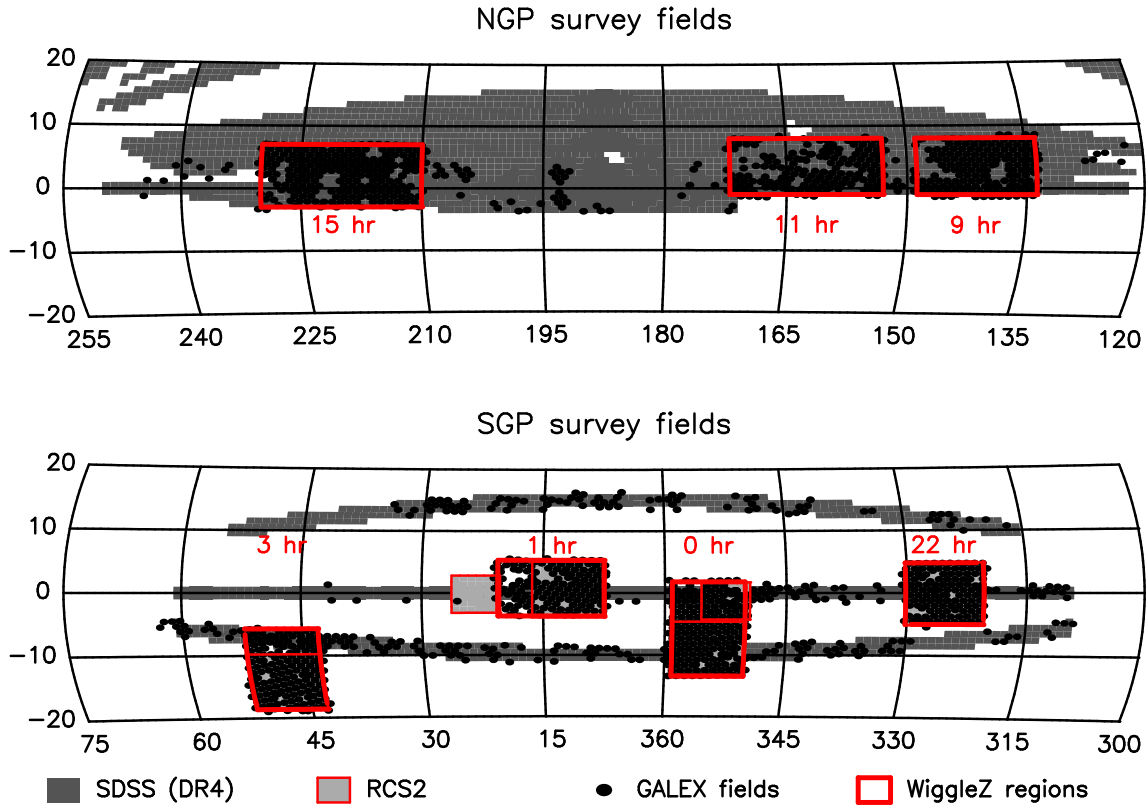


**Figure 1.** The sky distribution of the seven WigglesZ survey regions compared to the coverage of the SDSS, RCS2 and GALEX data sets at the end of 2008.

**Table 1.** Design of the Observational Programme

Component	Value
Success rate (fraction $Q \geq 3$ )	60%
Target fibres/field	325
Fields/ clear night	7.4
<b>Rate (successful targets/night)</b>	<b>1442</b>
Required number of targets	240,000
Rate per night (from above)	1442
Required clear nights	166
Weather factor	1.33
<b>Required total nights</b>	<b>221</b>

**Table 2.** Survey Regions: Full Extent

Name	$RA_{min}$ (deg)	$RA_{max}$ (deg)	$Dec_{min}$ (deg)	$Dec_{max}$ (deg)	Area (deg <sup>2</sup> )
0-hr	350.1	359.1	-13.4	+1.8	135.7
1-hr	7.5	20.6	-3.7	+5.3	117.8
3-hr	43.0	52.2	-18.6	-5.7	115.8
9-hr	133.7	148.8	-1.0	+8.0	137.0
11-hr	153.0	172.0	-1.0	+8.0	170.5
15-hr	210.0	230.0	-3.0	+7.0	199.6
22-hr	320.4	330.2	-5.0	+4.8	95.9

BAO scale. For this we need to obtain as many high redshift galaxy redshifts as possible per hour of AAT observing without necessarily obtaining a sample with simple selection

**Table 3.** Survey Regions: Priority Areas

Name	$RA_{min}$ (deg)	$RA_{max}$ (deg)	$Dec_{min}$ (deg)	$Dec_{max}$ (deg)
0-hr	350.1	359.1	-13.4	-4.4
1-hr	7.5	16.5	-3.7	+5.3
3-hr	43.0	52.2	-18.6	-9.6
9-hr	135.0	144.0	-1.0	+8.0
11-hr	159.0	168.0	-1.0	+8.0
15-hr	215.0	224.0	-2.0	+7.0
22-hr	320.4	330.2	-5.0	+4.8

Note: the high-priority region of the 22-hr field is the full field.

criteria in all the observing parameters. We nevertheless discuss the selection process in detail in this section to facilitate the use of the WigglesZ data for other projects that may need well-defined (sub) samples.

### 3.1 GALEX ultraviolet imaging data

Our target galaxies are primarily selected using UV photometry from the GALEX satellite (Martin et al. 2005). This satellite is carrying out multiple imaging surveys in two ultraviolet bands, in FUV from 135–175 nm, and in NUV from 175–275 nm. Specifically, the WigglesZ survey uses the photometry of the GALEX Medium Imaging Survey (MIS), which is an imaging survey of 1,000 square degrees of sky to a depth of 23 mag in both bands. The MIS consists of observations of 1.2 degree diameter circular tiles, with a nominal minimum exposure time of 1500 seconds. Several hun-

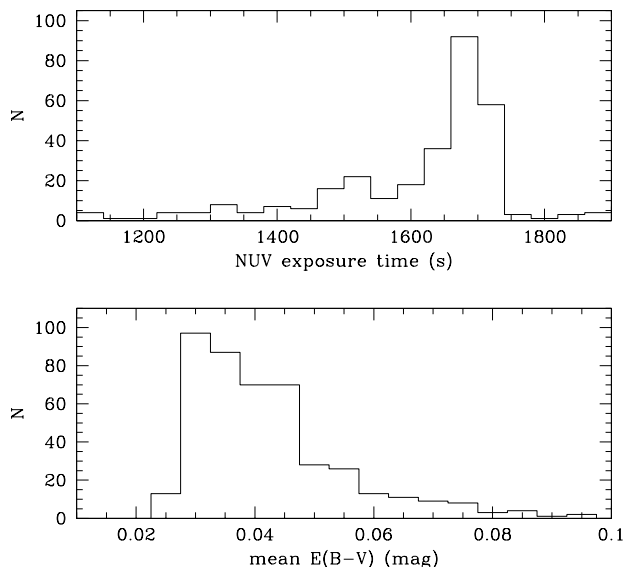


**Figure 2.** Properties of GALEX data used to select WiggleZ targets. Upper panel: distribution of exposure times. Lower panel: distribution of average dust extinction of each tile.

dred extra GALEX observations will be dedicated to the WiggleZ project. These are in addition to the original MIS survey plan, but they are all taken with the standard MIS-depth exposures and cover more contiguous sky areas due to improved bright-star avoidance algorithms. Furthermore, GALEX observations in the original MIS plan that overlap the WiggleZ survey regions are being observed at a higher priority to maximise the fields available for the WiggleZ survey.

The MIS data we use for WiggleZ have a range of exposure times, as illustrated by the distribution shown in Figure 2. The sharp peak at 1700 seconds arises because this is the maximum possible observing time in one satellite orbit. The figure also shows that there is a range in average Galactic dust extinction across the different GALEX observations. The effect of dust is discussed in Section 3.4 below.

All GALEX observations for the WiggleZ project are processed by the standard MIS data pipeline at Caltech to produce image catalogues (Morrissey et al. 2007). The NUV images are processed in a standard way with objects detected according to a threshold criterion using SExtractor (Bertin & Arnouts 1996). For the NUV detections we use the “NUV calibrated magnitude” from the pipeline: this is the flux through an elliptical aperture scaled to twice the Kron radius of each source (termed “MAG\_AUTO” by SExtractor). The detection limit in the raw NUV data is about 23 mag, as shown in Fig. 4 (a). We used a different approach for the FUV photometry because relatively few objects at the faint limit of our survey ( $NUV \approx 22.8$ ) were independently detected in the FUV band in the relatively short MIS exposures. We therefore based the FUV photometry entirely on the NUV detections. For each object in the NUV catalogue, the corresponding FUV magnitude is obtained by measuring a fixed 12-arcsecond (8 pixel) diameter circular aperture (“aperture 4” in the pipeline) in the FUV

image at the NUV position. The full width half-maximum (FWHM) of the GALEX point spread function (PSF) is 4.3 arc seconds in the NUV and 5.3 arc seconds in the FUV. Our use of total NUV magnitudes and aperture FUV magnitudes means that our  $FUV - NUV > 1$  colour selection could, in principle, be biased by colour gradients in resolved sources. Similarly we could suffer from source confusion with objects separated in the NUV data still being close enough to contaminate the FUV apertures, causing objects to incorrectly not satisfy the FUV-NUV colour limit (see Section 3.5). In practice, the low FUV signal means that very few sources are rejected by this colour criterion. The  $1-\sigma$  calibration uncertainties in the GALEX photometry are 0.05 and 0.03 magnitudes in the FUV and NUV bands, respectively (Morrissey et al. 2007).

The astrometric precision of the MIS catalogue positions is 0.5 arc second r.m.s., but this worsens with increasing distance from the centre of a tile (Morrissey et al. 2007). The nominal FWHM of the PSF of 5 arc seconds also becomes poorer at increasing distance from the centre of a tile. Additionally, uncertainties in the photometric zero-points of the GALEX observations increase radially from the tile centre. For these reasons, the WiggleZ survey only utilises the inner 1.1 degree diameter region of each GALEX tile, where the astrometry, PSF and photometric zero-point uncertainties are negligibly different to the nominal values.

At UV wavelengths, it is especially important to correct the photometry for Galactic dust extinction. The standard GALEX pipeline records the  $E(B - V)$  extinction (Schlegel, Finkbeiner, & Davis 1998, hereafter SFD) for each detected source. We then apply the following corrections (including zero-point calibration to the AB system) to the NUV and FUV photometry (Wyder et al. 2007):

$$FUV = FUV_{raw} + 18.82 - 8.2 \times E(B - V) + 0.06 \times E(B - V)^2, \quad (1)$$

$$NUV = NUV_{raw} + 18.82 - 8.2 \times E(B - V) + 0.67 \times E(B - V)^2. \quad (2)$$

We note that the SFD dust maps have a resolution of 6.1 arc min and that the uncertainty in the reddening values is 16%. We also note that SFD determined that it was not reliable to calibrate the dust map normalisation from variations in the number counts of optically-selected galaxies: this overestimates the dust amplitude because typical galaxy catalogues are both magnitude and surface brightness limited. We further discuss the sensitivity of our image catalogues to dust in Section 3.4.

### 3.2 Optical Data

In addition to the GALEX photometry, we use optical photometry from the fourth data release of the Sloan Digital Sky Survey (SDSS, Adelman-McCarthy et al. 2006) and from the CFHT Second Red-sequence Cluster Survey (RCS2, Yee et al. 2007) to provide accurate astrometry and improved target selection.

The SDSS photometry covers 7,000 square degrees of sky in 5 bands from the near ultraviolet to the near infrared. The five bands are  $u, g, r, i$  and  $z$ , with magnitude limits (95 per cent point source completeness) of 22.0, 22.2, 22.2, 21.3 and 20.5 mag respectively. The median PSF FWHM (in  $r$ )

is 1.4 arc seconds. The photometric calibration of the SDSS is nominally accurate to 0.02–0.03 magnitudes (Ivezić et al. 2004), but the uncertainty at our faint detection limit of  $r = 22.5$  is more likely to be 0.2–0.3 magnitudes. We use the SDSS “model” magnitudes, calculated on the AB system. The location of objects detected in these bands is known to an rms astrometric accuracy of 0.1 arc seconds.

The RCS2 is an imaging survey of 1,000 square degrees of sky in 3 of the SDSS bands:  $g$ ,  $r$  and  $z$ . The magnitude limits (5-sigma point source limits) are 25.3, 24.8, and 22.5 respectively, significantly fainter than in the SDSS. The typical seeing in the RCS2 imaging is  $(0.6 \pm 0.1)$  arc seconds for the best half of the data and  $(0.8 \pm 0.1)$  arc seconds for the remainder. The internal photometric precision of the RCS2 is close to that of the CFHT Legacy Survey (Ilbert et al. 2006), i.e. 0.04 mag in each band; the magnitudes are on the AB system, calculated from a curve-of-growth analysis. The colours are measured in smaller (adaptive) apertures and then scaled to the total magnitude of the source in the band with the strongest detection (usually  $r$ ). The RCS2 has an astrometric accuracy of 0.15 arc seconds, comparable to the astrometric precision of SDSS.

The precise astrometry of both these optical data sets is crucial to the WiggleZ survey, because the combination of the point-spread-function and astrometry of the GALEX source detections is too poor for the optical fibres used to feed light into the AAOmega spectrographs, which subtend an angle of 2 arc seconds on the sky. In all our processing we use dust-corrected optical catalogues. For SDSS, the dust correction is provided as part of the public data and for RCS2 we apply a dust correction ourselves: in both cases this is the standard SFD correction.

### 3.3 Matching UV to optical samples

The WiggleZ targets are selected from the GALEX UV photometry and then combined with either SDSS or RCS2 optical photometry. In the NGP region we combine the GALEX photometry with SDSS photometry, and in the SGP region we combine it with RCS2 photometry. The respective catalogues are combined by selecting the closest optical match to each GALEX source within a radius of 2.5 arc seconds. For the surface densities of the three data sets, this corresponds to 95 per cent confidence in a GALEX-SDSS match and 90 per cent confidence in a GALEX-RCS2 match. (The lower confidence for the RCS2 matches is mainly a consequence of the higher number density of sources in the RCS2 data.) We use the optical position for each matched source in our target catalogues as these are more precise than the GALEX positions.

Once an object is matched to the optical data, we can then apply further colour limits to refine our colour selection (see Section 3.5) noting that the  $NUV - r$  colour is a total colour. However, the large size of the GALEX PSF (FWHM 4.3 arc seconds in the NUV) compared to the optical imaging means that the colours may be distorted if multiple objects are merged in the GALEX photometry, but are resolved in the optical imaging. In this case the GALEX photometry would be too bright compared to the optical measurement. As discussed in Section 6.2, this is possible given the evidence for multiple sources we present in Fig. 18.

### 3.4 Uniformity of GALEX Data

An important requirement for the survey is that no artificial structure be introduced by variations in the input catalogues. This is particularly true for the GALEX data as the tile diameter (1.1 degrees) is close to the BAO scale (see Section 2). The primary source of non-uniformity is likely to be foreground Galactic dust, although we also test the data for any calibration offsets. To demonstrate the importance of dust, we show the range of *average* dust extinction across each tile, for a set of GALEX tiles in Fig. 2 (lower panel). This range ( $0.03 \lesssim E(B - V) \lesssim 0.07$ ; see Section 3.1 for the conversion to  $A_{NUV,FUV}$ ) is sufficient to affect the detection rates as we show below. In Fig. 3 we present images of the SFD dust maps in each field. These clearly show structure on scales similar to and smaller than the BAO scale, so it is very important to quantify the effect of dust on our input catalogues and correct for it if necessary. We also note an additional effect: some of the regions of higher dust are associated with Galactic nebular emission. One such example is the Eridanus loop which coincides with the diagonal dust lane visible in the 3-hour field in Fig. 3. Spectra of targets in such regions can be contaminated by rest-wavelength nebular emission lines, confusing the target redshift measurement.

We tested the GALEX photometry in two ways: first by analysing the detected number counts and secondly by comparing the photometry of objects measured in overlapping GALEX tiles. The first test addresses all factors affecting image detection (notably dust) and the second tests the internal calibration of the photometry. The second tests did not reveal any evidence for significant differences in absolute calibration between overlapping tiles, so these will not be discussed in any more detail (small offsets were measured, but these were uncorrelated the numbers of images detected on the respective tiles).

In Figure 4(a,b) we show the differential number counts of all sources detected in the NUV tiles in the 15-hour region. In the upper panel the counts are plotted as a function of raw observed magnitude and in the lower plot, as a function of dust-corrected magnitude. In each case the tiles are grouped according to the average dust extinction for each tile and the lines plotted give the average counts for each group of tiles as indicated by the key. We further limited the choice of tiles to those with exposures in the range 1600–1700 seconds to focus on the role of extinction. Our first observation from the plots is that the dust correction is working as expected: the uncorrected counts all show the same faint cut-off in raw magnitude, but they have different normalisations of their power-law slopes. In contrast, the dust-corrected counts show the same power-law normalisation, as desired.

Although we have shown that calibration variations in the GALEX data are minimal, the faint magnitude cut off in the counts has a strong effect on the number of WiggleZ targets selected as shown in Fig. 4(c,d). Here we show the number counts of WiggleZ targets, having applied the survey selection criteria (see Sec. 3.5) to the raw counts. This shows that, unlike the raw counts, the WiggleZ target counts at our survey limit ( $NUV < 22.8$ ) are strongly affected by dust. The mean counts per tile vary by a factor of two over the full range of extinction, although 70 per cent of the tiles lie

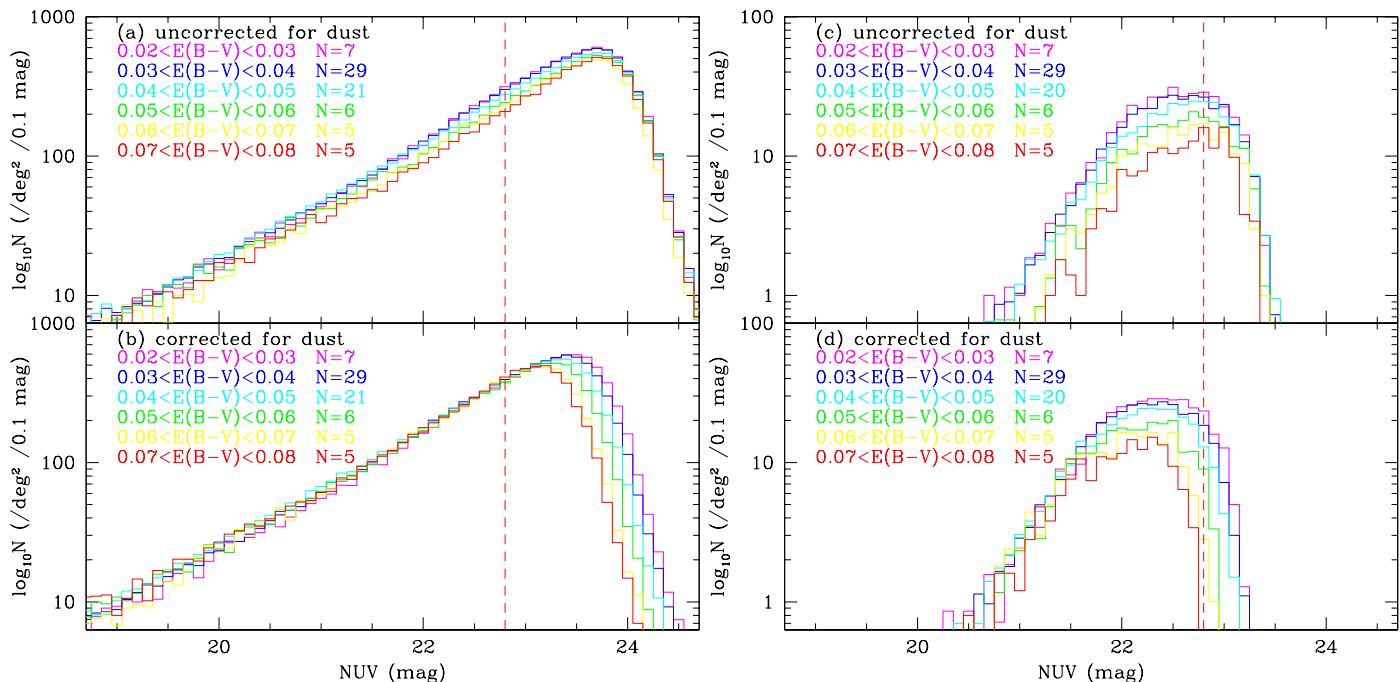


**Figure 4.** Number counts of GALEX NUV detections in tiles from the 15-hour region as a function of dust extinction. The NUV magnitude limit of the WiggleZ survey is indicated by a vertical dashed line in each plot. In the left hand panels (a, b) we plot all objects detected before and after the dust correction. The counts are binned by the average dust extinction in each tile, one curve for each bin (see key). The upper panel shows the raw counts; in the lower panel the dust correction has been applied to every individual object. The improved agreement of the power-law region of the number counts in panel b demonstrates the effectiveness of the dust correction. The right hand panels (c, d) are similar, but only count objects that satisfy the WiggleZ target selection criteria. Panel d shows that the target numbers at the NUV survey limit are more sensitive to dust than the total counts of detections shown in panel b.

in a narrow range of extinction ( $0.025 < E(B - V) < 0.045$ ) for which the counts vary by only 10 per cent. For the WiggleZ clustering measurements we will deal with this effect by scaling the random catalogues to follow the GALEX magnitude limits. We have tested this approach by measuring the angular power spectrum of the galaxies and comparing that to theoretical models. After scaling our selection function to allow for the combined effects of dust and exposure time on the GALEX counts we find there is no evidence for any large-scale systematic variation (Blake et al. 2009a). For measurements of the luminosity function of the WiggleZ sources, however, the correction needs to be with respect to the underlying power law and is therefore much larger. This will be discussed in more detail in later papers.

### 3.5 Galaxy Selection

The main criteria used to select the WiggleZ survey targets from the GALEX and optical photometry are a  $FUV - NUV$  colour cut to select high-redshift galaxies, and a  $NUV - r$  colour cut to select emission line galaxies. These are shown in Fig. 5, a colour-colour plot of  $FUV - NUV$  vs.  $NUV - r$ . In the diagram we show the WiggleZ selection limits (dashed rectangle), data points from combined DEEP2 (Davis et al. 2003) and GALEX observations, and model tracks for several galaxy types over a range of redshifts.

The UV colour selection (specifically  $FUV - NUV \geq 1$  or  $FUV$  undetected: a “drop-out”) selects galaxies at red-

shifts  $z \geq 0.5$  because the Lyman break enters the FUV filter at a redshift of  $z \approx 0.5$ . We note that in the MIS UV data used in our survey, for fainter galaxies (near our NUV detection limit), the  $FUV$  measurements have very low signal-to-noise, so the drop-out selection criterion is very crude. (The data points in Fig. 5, by contrast, were measured in much deeper GALEX data than used for our survey.)

The diagram also shows how we use the  $NUV - r$  colour. The  $NUV - r \leq 2$  limit selects bluer star-forming galaxies, and the  $-0.5 \leq NUV - r$  limit helps remove spurious matches between the GALEX and optical data sets. These two colour cuts were chosen based on the colours of galaxy models as a function of redshift. The colours of these galaxy models and the colour cuts used for the WiggleZ target selection are shown in Fig. 5.

For the GALEX NUV photometry we impose a faint magnitude limit of 22.8 in NUV. In addition, we also require that the NUV flux measurement has a signal-to-noise  $\geq 3$  to minimise the number of false detections. This requirement becomes increasingly important for dustier regions of the sky: in regions of low dust ( $E(B - V) \approx 0.03$ ) the signal-to-noise cut removes about 10 per cent of the raw  $NUV \leq 22.8$  sources, but in high dust regions ( $E(B - V) \approx 0.06$ ) it removes 25 per cent of the sources.

For the optical photometry (both SDSS and RCS2) we impose a magnitude range of  $20 < r < 22.5$ . The faint limit is set by the SDSS survey detection limit; the bright limit is to avoid low-redshift galaxies. As a consequence of this

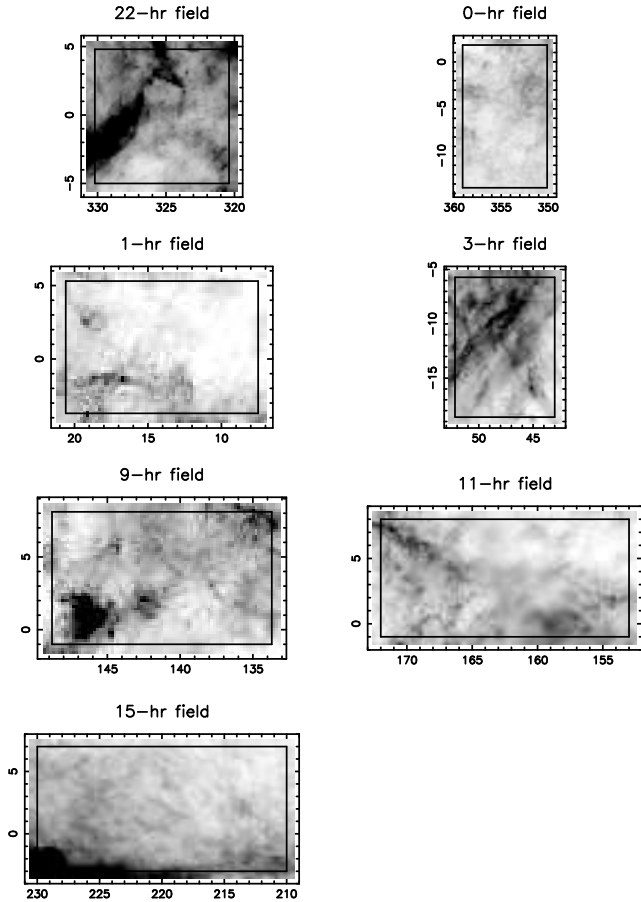


**Figure 3.** Distribution of dust in each of the survey fields. The grey scale shows the Schlegel, Finkbeiner, & Davis (1998) extinction values such that white is  $E(B - V) = 0.02$  and black is  $E(B - V) = 0.1$ . The horizontal and vertical axes in each panel denote the Right Ascension and Declination, respectively, measured in degrees.

bright  $r$  magnitude limit, the  $NUV - r$  colour cut results in a bright magnitude limit in the  $NUV$  of 19.5, although this is not explicitly part of the WiggleZ target selection criteria. A further consequence of the  $NUV - r$  colour cut (and indeed the average  $NUV - r$  colours) is that the optical magnitudes of the selected galaxies do not peak at the faint  $r = 22.5$  limit, but instead peaks at  $r \approx 21.5$ , about a magnitude brighter. Note that we do not apply any morphological selection to remove objects classified as “stellar” in the optical imaging because virtually no stars satisfy our photometric selection criteria. These basic selection criteria are listed in the first section of Table 4.

A further selection based on optical colour is used to reduce the number of targets selected with redshifts below  $z = 0.5$ . These arise because the  $FUV - NUV$  selection is imperfect due to photometric errors — many of our targets are at the limits of the GALEX photometry in typical MIS exposures. We do this by rejecting galaxies whose optical colours and magnitudes indicate they are very likely to be lying at lower redshifts (as shown in Fig 6). Two different sets of low redshift rejection (LRR) criteria are used in the SDSS and RCS2 regions respectively, as listed in Table 4. In the SDSS data we are near the faint limit of the survey,

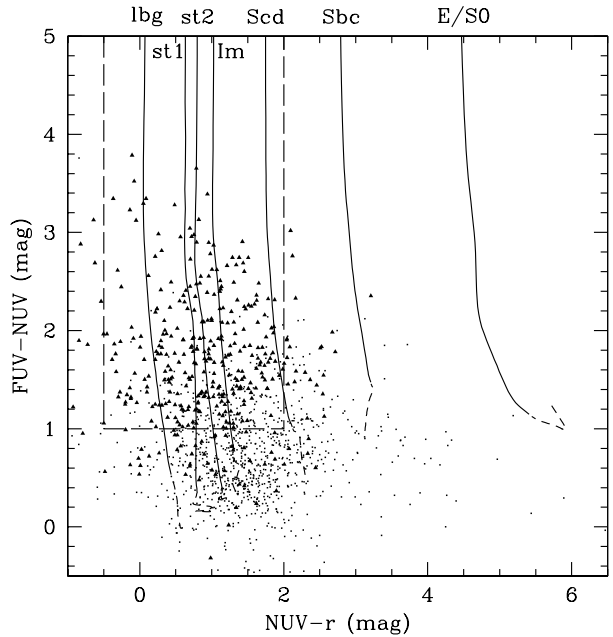


**Figure 5.** The basic WiggleZ target selection criteria. The rectangle marked by the dashed line denotes the region in  $FUV - NUV, NUV - r$  colour space where WiggleZ targets lie. The solid lines are the model tracks for seven galaxy templates as a function of redshift for  $z > 0.5$ . The first track, from left to right, is for a Lyman break galaxy template (Figure 1 in Steidel et al. 1996). The remaining tracks are two starburst templates (Kinney et al. 1996) and a series of (Im to E/S0) local galaxy templates (Coleman, Wu, & Weedman 1980), all extended in wavelength range by matching them with Bruzual & Charlot (1993) models (Hsaio-Wen Chen, private communication). The dashed lines at the end of the solid lines are these models for  $z \leq 0.5$ . Also shown as points are galaxies from deep GALEX imaging that were detected in all three bands and have published redshifts from the DEEP2 survey (Davis et al. 2003). The triangles indicate objects with redshift  $z > 0.5$ .

so can only apply this to the brighter galaxies. However the brighter galaxies are more likely to be at lower redshift so this ameliorates this disadvantage. We therefore start by applying  $g$  and  $i$  magnitude limits in order to secure accurate colours. Then we apply a  $(g - r, r - i)$  colour cut to select the 400 nm break in galaxies at redshifts  $z < 0.5$ . In the RCS2 regions the optical data go much deeper, so no magnitude limits are required, but there are no  $i$  data, so we have to use a  $(g - r, r - z)$  colour cut which is less precise at discriminating at  $z < 0.5$ . The success of these selection criteria is demonstrated in Fig. 7 where we show redshift distributions of the objects observed with and without the LRR colour cuts.

We also apply a prioritisation scheme to our target allocation as given in Table 5. The priorities given in the table are used when observing so that higher-priority objects are observed first. This is done for two reasons. First, there is a weak correlation between  $r$  magnitude and redshift (shown in Fig. 8) so this also serves to select high-redshift objects. Secondly, this approach means that our later observations will be of brighter objects, allowing us more flexibility in the final stages of the observational campaign.

Before observing we make a final check of all the tar-



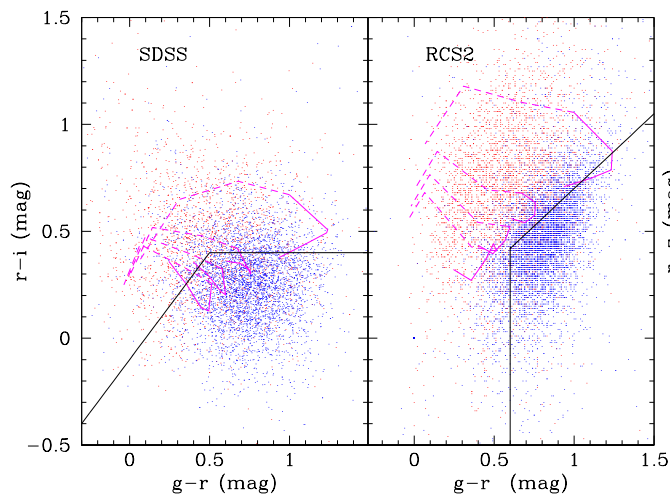


**Figure 6.** The selection criteria applied to avoid low-redshift targets in the two survey regions. The points in each diagram are WiggleZ galaxies observed before we introduced the low redshift rejection cuts. Galaxies with redshifts below  $z = 0.6$  are plotted as blue points; the rest are plotted in red. Galaxies below the lines in each panel are rejected from the target catalogue as they have a high probability of being at low redshifts. Also shown as magenta lines are PEGASE-2 (Fioc & Rocca-Volmerange 1997) evolutionary tracks of four galaxy models ranging from E/SO (upper) to Irr (lower) types. Each model ranges from  $z = 0$  to  $z = 1$  with the high redshift ( $z > 0.5$ ) section dashed.

**Table 4.** Photometric selection criteria for WiggleZ galaxies

Criterion	Values
<i>Select targets satisfying all these basic criteria:</i>	
Magnitude	$NUV < 22.8$
Magnitude	$20 < r < 22.5$
Colour	$(FUV - NUV) > 1$ or no FUV
Colour	$-0.5 < (NUV - r) < 2$
Signal	$S/N_{NUV} > 3$
Optical Position	matches within 2.5 arc seconds
<i>Then reject targets satisfying these:</i>	
$LRR_{SDSS}$	$g < 22.5, i < 21.5,$ $(r - i) < (g - r - 0.1), (r - i) < 0.4$
$LRR_{RCS2}$	$(g - r) > 0.6, (r - z) < 0.7(g - r)$

get objects by visually inspecting them on SuperCOSMOS (Hambly et al. 2001) sky survey images to ensure none are artifacts associated with extremely bright ( $r < 12$ ) Galactic stars. This happens occasionally with automated data catalogues because bright objects can be incorrectly segmented into smaller, fainter objects, which are then matched to GALEX NUV detections. This is a problem, because the signal from these bright objects swamps adjacent spectra in such a way that we lose as many as 30 spectra from an observation.

The final result of the whole selection process is a target catalogue with an average surface density of  $350 \text{ deg}^{-2}$  which is well matched to our survey goals. The WiggleZ target galaxies represent a small fraction of optical galaxies. Analysis of a sample of DEEP2 (Davis et al. 2003) galaxies for which deep optical and GALEX observations are available

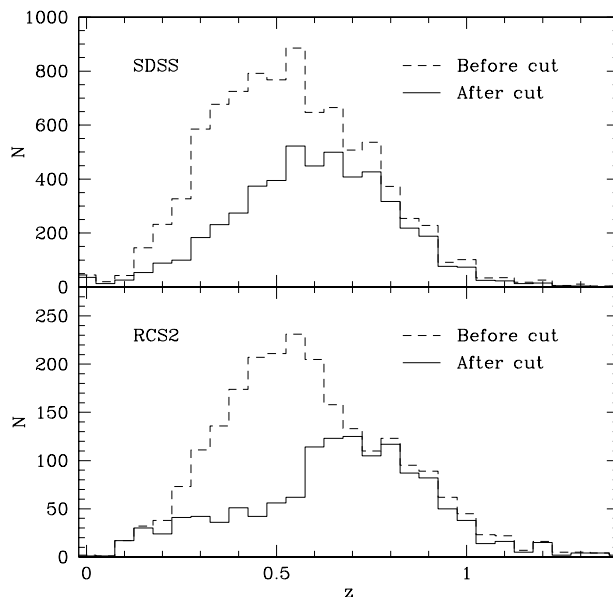


**Figure 7.** The result of the optical colour cuts used to reduce the number of low-redshift targets. The top panel shows the effect in the Northern (SDSS) regions of the survey and the lower panel shows the Southern (RCS2) regions. In each panel the dashed histogram shows the redshift distribution of all galaxies observed before the dates on which the colour cuts were applied in each section of the survey (see dates in Table 7). In each panel the solid histogram shows the results of retrospectively applying the colour cuts to these same objects. In both regions the cuts result in a significantly higher median redshift; we note that the deeper photometry in the RCS2 regions allows a more effective cut to be applied in the lower panel.

**Table 5.** Priority selection scheme for WiggleZ observations

Criterion	Priority
repeat observations	9 (highest)
white dwarf calibrators	9
<i>New targets<sup>1</sup> by magnitude:</i>	
$22.0 < r < 22.5$	8
$21.5 < r < 22.0$	7
$21.0 < r < 21.5$	6
$20.5 < r < 21.0$	5
$20.0 < r < 20.5$	4
<i>Other objects:</i>	
Additional projects	3
Old good weather targets ( $Q = 1,2$ )	2
Old good weather targets ( $Q = 3-5$ )	1 (lowest)

Note 1: The “new” targets include objects that were previously observed in bad weather without obtaining a redshift.

shows that in the SDSS regions, WiggleZ selects  $2.2 \pm 0.2$  per cent of the ( $r < 22.5$ ) optical galaxies. In the RCS2 regions, WiggleZ selects  $2.6 \pm 0.2$  per cent of these same galaxies. These low percentages are mainly due to the WiggleZ NUV flux limit and  $NUV - r$  colour cuts which only select galaxies with very high current star formation rates, but we also note that the median  $r$  magnitude of the WiggleZ galaxies is brighter than  $r = 22.5$  (see Fig. 8).

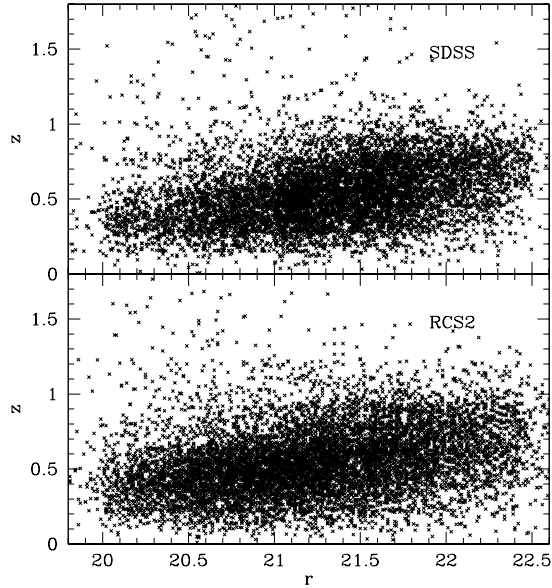


**Figure 8.** The correlation between redshift and  $r$ -band flux for the observed WiggleZ galaxies. As there is a weak correlation in both the SDSS (top panel) and RCS2 (lower panel) samples, we observe targets with fainter  $r$  magnitudes at a higher priority in order to increase the median redshift of the sample.

#### 4 SPECTROSCOPIC OBSERVATIONS

The major component of this project is our large, 220-night observing campaign on the AAT. In this section we describe the management of this campaign, the procedures required to configure our AAOmega observations and the data processing.

##### 4.1 AAOmega Spectrograph and Observing Setup

The efficiency of the WiggleZ redshift survey is critically dependent on the high sensitivity and multiplexing gain made possible by the new AAOmega spectrograph and existing 2dF fibre positioner on the AAT (Smith et al. 2004; Saunders et al. 2004). AAOmega is a bench-mounted, fibre-fed spectrograph consisting of blue and red arms split by a dichroic. Volume phase holographic (VPH) gratings are utilized resulting in an improved efficiency over reflection gratings. The bench for the spectrograph is mounted in a mechanically and thermally stable coudé room. For more details about the performance characteristics of AAOmega, see Sharp et al. (2006).

In multi-object mode the combination of the 2dF positioner and AAOmega spectrograph allows observations with a total of 392 fibres over a circular field of view with a diameter of two degrees. The angular size of each fibre on the sky is 2 arc seconds. Our survey utilizes the 580V and 385R gratings in the blue and red arms, respectively, both providing a resolution of  $R \approx 1300$ . This gives a dispersion of about  $0.11 \text{ nm pixel}^{-1}$  in the blue arm and  $0.16 \text{ nm pixel}^{-1}$  in the red arm.

The observable wavelength range of the system is 370–950 nm. The blue limit is determined by the fibre transmis-

**Table 6.** The two AAOmega setups used for our observations

Dichroic	$\lambda_{C,Blue}$	Blue Range	$\lambda_{C,Red}$	Red Range
570 nm (old)	477	370–580	725	560–850
670 nm (new)	575	470–680	815	650–950

Note: for each dichroic the table lists the central wavelength setting and observable wavelength range for the blue and red arms of the spectrograph. For each VPH grating the blaze wavelength was set to be the same as these central wavelengths for maximum efficiency. All units are nm.

**Table 7.** Significant Dates in our Observing Campaign

Date	Activity	$N_z$
2006 February	Pilot observations	
2006 August 19	Start of survey (semester 2006B)	
2007 April 11	Start of using LRR in SDSS fields	12445
	Start of 0.7 deg radius observing	
2007 June 8–21	Observations without blue camera	24740
2007 August 7	Start of new dichroic use	26293
2007 August 14	End of 0.7 deg radius observing	38540
2007 October 4	Start of using LRR in RCS2 fields	42179
2008 May 13	End of Semester 2008A and half-way point after 112 nights.	100138

Note:  $N_z$  is the running total number of good redshifts ( $Q \geq 3$ ) measured on each date.

sion characteristics (over the 38m-long fibres) and the red limit is due to the CCD response. In our early observations, we used the standard dichroic with the cut over centred at 570 nm. As we also required a small spectral overlap between the blue and red arms, this fixed the low-wavelength limit of the red spectrograph which could then only cover up to a maximum wavelength of 850 nm. We alleviated this limit on observing redder wavelengths by purchasing a new dichroic for AAOmega, in partnership with the AAO, to extend our wavelength coverage.

The original AAOmega dichroic beam splitter cuts over at 570 nm while the new dichroic has a cut over at 670 nm. The new dichroic was specially designed for our project to allow improved spectral coverage out to the system limit of 950 nm, using the 385R grating, while still allowing continuous spectral coverage down to a new blue limit of 470nm (see Table 6). This redder wavelength range enables more reliable redshift identification of the emission-line galaxies in our sample. Specifically, an increase of 100 nm at the red end allows the detection of secondary emission-lines such as  $H\beta/[OIII]$  lines at higher redshifts up to  $z \approx 0.95$ . At redshifts above  $z \approx 0.95$  we often rely on just the [OII] (372.7, 372.9 nm) doublet for redshift identification, but we are aided by the fact that the doublet is often resolved at these redshifts. The new dichroic was first used for our 2007 August observing run (see Table 7). About 25 per cent of the 100,138 reliable redshifts measured up to the end of Semester 2008A on 2008 May 15 were taken with the original dichroic; the rest used the new dichroic which will be used for the remainder of the survey.

## 4.2 Blank Sky and Guide Star Positions

The 2dF/AAOmega system, like other multi-object fibre spectrographs requires fiducial (“guide”) stars to align the field accurately and blank sky positions where a subset of the target fibres can be placed to sample the sky background.

### 4.2.1 Selection of Blank Sky Positions

The blank sky positions must satisfy two criteria: their number density on the sky should be high enough to ensure we can always configure at least 25 sky positions in any given 2dF observation, and each must be sufficiently far from any other object on the sky to avoid contamination. We chose a density of 40 sky positions per square degree, corresponding to 120 per 2dF observation. This was judged to be sufficient to allow 25 sky fibres to be configured after all the target and guide fibres were positioned.

We selected the sky positions automatically from the image catalogues for each region by setting down a square grid of the desired surface density. Any grid positions too close to a catalogue image were moved (randomly) within the corresponding grid cell as necessary until they satisfied a proximity test. The proximity test for neighbouring objects was a function of their apparent  $r$  (or  $R$ ) magnitude: the sky position was moved if there were neighbours satisfying  $r < 12.5$ ,  $r < 16$ ,  $r < 17.5$ , or  $r \geq 17.5$ , within distances of 1.5, 1, 0.5, or 0.25 arc minutes respectively.

### 4.2.2 Selection of Guide Star Positions

The guide stars for AAOmega must satisfy strict photometric and astrometric criteria. Most importantly, their positions must be accurate and on the same reference frame as the target objects. The new 2dF/AAOmega system has 8 fibre guide bundles on each plate so, in principle, observations are still possible if one or two of the guide stars are not suitable. However the diagnosis of the defective stars slows down the observing process, to the extent that they would amount to a significant time loss over the course of a large survey like WiggleZ.

To satisfy the astrometric criterion we selected guide stars from different sources in each of the two survey regions. In the northern SDSS survey regions we selected guide stars directly from the same SDSS catalogues as we used for our optical target photometry. We used the SDSS automated image classification flags to select stars from the catalogues (“mode”=1, “type”=6, “probPSF”=1).

In the southern (RCS2) regions we were unable to obtain guide star positions from our imaging data as they are much deeper and hence most guide stars are saturated, so they have unreliable positions. We therefore chose guide stars for these regions directly from the USNO-B astrometric catalogue (Monet et al. 2003) which was used to provide the astrometry for the RCS2 data (with fainter USNO-B stars that were not saturated in the RCS2 images). We undertook extensive testing of the USNO-B guide star astrometry, comparing the positions to both SDSS data (in the limited regions where they overlap) and also with the all-sky 2-MASS catalogue data (Skrutskie et al. 2006). In the regions tested we found small but significant systematic position differences between 2-MASS and USNO-B; for the

**Table 8.** Astrometry Offsets in RCS2 Regions

Name	$RA_{USNO} - RA_{2MASS}$ (arc seconds)	$Dec_{USNO} - Dec_{2MASS}$ (arc seconds)
0-hr	$-0.112 \pm 0.003$	$0.117 \pm 0.003$
1-hr	$-0.133 \pm 0.004$	$0.102 \pm 0.003$
3-hr	$-0.141 \pm 0.002$	$-0.026 \pm 0.002$
22-hr	$-0.031 \pm 0.003$	$0.137 \pm 0.003$

SDSS versus 2-MASS comparison, we found no systematic difference. In all cases the r.m.s. scatter in the position differences (less than 0.2 arc seconds in each coordinate) was consistent with the published uncertainties in the respective catalogues. The offsets are tabulated in Table 8. We have not adjusted the RCS2 or USNO-B astrometry for the small systematic offsets with respect to the SDSS/2-MASS astrometry, as this is not necessary for our spectroscopic observations. There is no measurable offset between the astrometry of the RCS2 data (our targets) and the USNO-B catalogue (our guide stars), so AAOmega observations using these guide stars will ensure the target fibres are correctly positioned.

We did find that the USNO-B guide star positions, when compared to 2MASS, displayed a measurable tail (1–2% of the total) in the distribution of position differences, with them being greater than 0.5 arcsec, a size not seen with the SDSS data. Inspection of the images in this tail showed many of these objects were not single stars, but galaxies or binary stars. We therefore imposed a further check on the USNO-B guide stars, that their positions had to be consistent with the corresponding 2MASS data (after adding the systematic offset to put them on the USNO-B system) to within 0.5 arc seconds. We did not apply any image classification test to the USNO-B stars as the classifications were less reliable than for SDSS and, at these magnitudes, the majority of images are stellar.

The guide star magnitudes for 2dF must be in the range 12–14.5 mag, and must not differ in brightness by more than 0.5 mag to not exceed the dynamic range of the guide camera. Since the WiggleZ project is conducted largely in the dark of moon, we opted for stars in the faintest range  $14 < r < 14.5$  to obtain as many as possible per field. In order to achieve good astrometry it is also important to avoid stars with high proper motion. We checked this using (USNO-B) catalogue data when available, but as a further check, we also avoided very red stars, as many of these are nearby M-dwarf stars which are more likely to have significant proper motions. The guide star selection criteria for the two survey regions are summarised in Table 9.

### 4.2.3 Visual Inspection

Finally, all the potential blank sky and guide star positions were inspected visually by team members, using SuperCOSMOS (Hambly et al. 2001) images at each position. This step is necessary because our input catalogues (like all automated image catalogues) suffer from a small rate of object mis-classification and even missing objects. These mistakes are not statistically significant, but could potentially ruin a complete observation.

**Table 9.** The selection criteria for guide stars

Criteria	SDSS	RCS2 (USNO-B)
Magnitude	$14 \leq r \leq 14.5$	$13.95 \leq R \leq 14.45$
Colour	$-0.5 \leq (g - r) \leq 1.5$	$-0.3 \leq (B - R) \leq 1.7$
Classification	stellar	any
Proper Motion	$p < 0.015$ arc seconds $\text{yr}^{-1}$	

For the sky positions, the visual check is simply to ensure there really is no object near the nominated position. The check is more demanding for the guide stars: we must ensure that they are really stellar, not multiple, and do not have any close neighbours (within about 30 arc seconds).

A total of some 50,000 different sky and guide star positions were defined across the different regions of the WiggleZ Survey, all of which were visually checked by a team member. To speed this process up, we designed a web-based interface that displayed large sets of SuperCOSMOS images, 1000 or more at a time, and allowed the team member to easily identify the small number of problematic positions.

### 4.3 2dF field placement

When the WiggleZ survey began taking data with AAOmega, the GALEX data set that formed the input catalogue for our survey was patchy and had a highly varying density of targets. Although both of these factors have since improved tremendously, we do not use a simple grid of 2dF field placements as it invariably produces highly pathological fields that the 2dF robotic positioner is unable to configure in sufficient time (i.e. less than the 1-hour typical observing time for each field).

Instead, we apply a simulated annealing algorithm to the problem of 2dF field placement. The algorithm used is identical to that used by Campbell et al. (2004) (see also Metropolis et al. 1953) for the 6dF Galaxy Survey (e.g. Jones et al. 2004), but modified for use with the 2dF system. Briefly, the algorithm generates an arrangement of 2dF placements that ensures that the smallest number of 2dF fields are used to give as large as possible coverage of the target set with as little variation in surface density as possible (see Fig. 9).

The annealing is performed prior to each observing run in order to have a fully efficient 2dF tile set to observe with. In practice, one issue that regularly arises with this process is that the annealing algorithm simply aims to fill each 2dF field with  $\sim 350^1$  fibres. In regions where the target density is high such that there are many more targets than the 350 the annealing algorithm is asked to assign fibres to, the result can potentially be a 2dF field where there is a large target density gradient within that field. This is especially true of areas that consist of a single, non-contiguous GALEX tile (Fig. 9)—the annealing algorithm does not know a priori to place the 2dF field such that it is centred on the GALEX

<sup>1</sup> We enter 350 fibres as the typical number of target fibres available per 2dF field. Combined with 8 guide star fibres, up to 25 sky fibres for sky subtraction and a variable number of broken fibres at any one time, 350 target fibres represents a good estimate as to the available number of fibres.

tile’s centre in order to make the fibre positioning run faster. Therefore we perform a small amount of manual intervention to optimize the resultant 2dF field placement by, for example, putting single GALEX fields in the middle of a 2dF circle. Our later publications (e.g. Blake et al. 2009b) will detail how we take account of the overlapping regions for the window function of our survey.

### 4.4 Observing priorities

The WiggleZ survey has seven equatorial fields roughly distributed over the full range of R.A. thus there are target fields readily available throughout the year. Of course, this will change as the survey progresses since more time will have to be expended on observations of the more incompletely sampled target regions. The target selection within a given WiggleZ survey region is necessarily complex due to the rapid evolution of our data set and the complicated selection criteria (Section 3.5). However, choosing an individual field pointing for a given night is mostly based on minimizing its hour angle over the course of the observation. Other factors typically considered when prioritizing field centres to be observed, include: (1) the field is part of a larger contiguous area in a WiggleZ region, (2) it contains a high target density (i.e., it will use all of the fibres), and (3) it does not lie on the edge of a GALEX tile or observed area (anticipating the GALEX data will be more contiguous in future observing runs).

### 4.5 Final target lists and calibration

Once the field pointings have been selected for a night of observing, combined target files for each field pointing are generated using custom software (developed by RJJ). These files combine the target galaxies (with suitable priorities assigned; see Table 5), guide stars, and blank sky positions. The software also reads the lists of objects observed earlier in the run to avoid repeat observations in overlapping regions. For the full 2-degree diameter field of view we generate a target file with an optimal number of 700–800 possible targets.

Our target catalogues are updated before each observing run to record which galaxies have already been observed. These are not normally re-observed with the exception that targets that were previously observed in poor conditions (typically with cloud cover more than 4/8 or seeing FWHM more than 3 arc seconds, resulting in a significantly reduced redshift completeness, less than 50 per cent) without obtaining an acceptable redshift are re-observed (see Table 5). Galaxies which were previously observed in good conditions are put in a reserve list and are occasionally re-observed at low priority ( $P = 2$  if no redshift was obtained;  $P = 1$  if a redshift was obtained).

A small number of additional calibration targets are included in the target file at high priority. First, where possible we include two standard stars: white dwarfs or hot sub dwarfs from the SDSS compilation by Eisenstein et al. (2006). These are used to assist in future spectrophotometric calibration. Secondly, in order to determine the reproducibility of our measurements, we include repeat observations of three previously allocated targets and three previously redshifted objects.

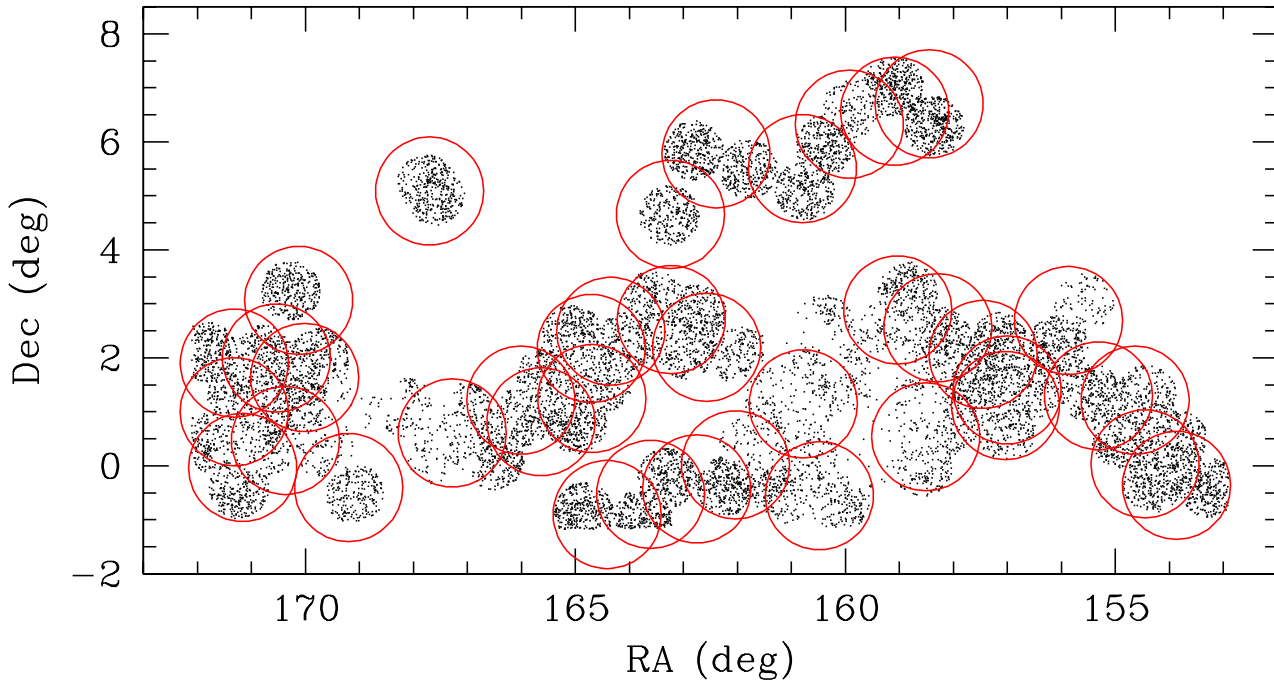


**Figure 9.** 2dF field placement for the 15hr rectangle resulting from simulated annealing prepared for the 2008 April observing run. The target set is non-uniform with significant areas of GALEX targets yet to be observed (blank areas) and a number of targets within the available GALEX tiles having already been observed in previous runs (e.g. note the apparent under-dense area at RA~160 and Dec~1). The simulated annealing approach ensures that a minimum number of 2dF positions is used to observe the targets.

In regions where we are unable to use all the fibres on high-priority WiggleZ targets, we allocate a small number of targets for companion projects to the main survey: candidate cluster galaxies from the RCS2 project and candidate radio galaxy identifications from the FIRST (Becker, White, & Helfand 1995) survey. These additional targets are placed at lower priority than all the new WiggleZ targets ( $P = 3$ ) and, in total, they account for less than 1 per cent of the observations made.

Finally, we note that a small number of the spectra from each plate at any time (up to 5 per cent) are affected by a fringing pattern superposed on the target spectrum. We are unable to measure redshifts for spectra strongly affected by the fringing. The interference fringing is caused by small air gaps between the ends of the 2dF fibres and the 90 degree prisms that collect the target light on the focal plane. The air gaps create etalons, introducing interference fringes which modulate the fibre transmission profile as a function of wavelength. The air gaps are the result of thermal expansion between the steel fibre mounts and the glass fibres themselves. The gap size is mechanically unstable, relaxing during each exposure after being disturbed during fibre placement, so the fringes are not removed by the flat field correction in the data reduction process. A hardware solution to the problem has been identified by the AAO, and will be applied in due course.

Allowing for the fringing fibres, as well as those devoted to background sky measurement and the various calibration measurements, the average number of fibres devoted to new

targets per observation in the survey data is 325 (as quoted in Table 1).

#### 4.6 Field configuration

The 2dF `CONFIGURE` software (Shortridge, Ramage & Farrell 2006) is then used to generate configuration files from the target lists. This optimally allocates all the fibres in use on the telescope to our targets. The configuration central wavelength is set to 670 nm due to our use of the new WiggleZ dichroic beam splitter. Within the `CONFIGURE` program, we generally choose to weight the peripheral fiducial targets, use 25 sky fibres in a pointing and enforce a sky fibre quota. A simulated annealing algorithm incorporated into recent versions (after v.7.3) of the `CONFIGURE` code (Miszalski et al. 2006) has greatly improved the yield of high priority targets and the spatial uniformity. Furthermore, high speed computers installed in the AAT control room in 2007 October, allow us to calculate optimal configurations for a typical field in less than half an hour.

The output of the `CONFIGURE` software is a configuration file specifying the position of every fibre, which is then used by the 2dF positioner to place all the fibres on the one of the two field plates that is to be used for the observation. The efficiency and reliability of the positioner was improved significantly during the first year of our observations, leading to positioner configuration times of less than one hour for all the fibres. These short configuration times provide greater observing flexibility, particularly during good observing con-

ditions. During these clear periods of good seeing we can then expose for less than our conventional one-hour exposure, and still obtain the appropriate signal-to-noise ratio required for successful target redshifting.

With a large number of observations now completed, we can illustrate the success of this process by plotting the physical positions of the fibres from all our observations. This is shown for both plates combined in Figure 10. Note that we have not included data taken in the period 2007 April to 2007 August; during this period we restricted our observations to a maximum radius of 0.7 degrees from the centre of each 2dF field as there was a problem with the astrometric calibration of the 2dF positioner which reduced the accuracy of fibre placement at larger radii.

The fibre distribution in Figure 10 reveals 8 areas of slightly lower density around the edge of the field, associated with the position of the 8 (equally spaced) fibre bundles used to measure the fiducial stars. A similarly weak effect was present in the 2dF Galaxy Redshift Survey (2dFGRS; Colless et al. 2001) but only 4 fiducial stars in that case). The 2SLAQ galaxy survey (Cannon et al. 2006), by contrast, had a very marked discontinuity at the field edges as only one of the 2dF spectrographs was used (alternate banks of fibres were used for the companion quasar survey). The fibre distribution in Figure 10 also displays a strong radial gradient in surface density. The average fibre density decreases by a factor of about 3 from the centre to the edge of the field. This is a natural consequence of the smaller size of the GALEX field compared to the 2dF field: in many observations we do not fill the edges of the 2dF field with targets.

#### 4.7 Data reduction

The AAOmega data are reduced during each observing run using the automated 2DFDR software developed at the AAO. We take standard calibration flat field tungsten and arc (CuAr, FeAr, Ne and He) exposures for each pointing throughout the night, whose integration times are typically 3sec and 30sec, respectively. A two-dimensional bias frame is constructed for the blue arm data to correct for a small number of high bias columns on the blue CCD.

The data from the blue and red arms for a field pointing are reduced separately, and then spliced together resulting in a final spectrum used for target redshifting. The high-speed computers available at the AAT make it possible to reduce the data in real time, allowing the observers to have the majority of the data ready for redshift measurement by the end of the night. We note that, as in the case of most fibre-fed spectroscopy, we do not flux calibrate the spectra. This is mainly due to the inherent difficulty in calibrating the fraction of total light collected by each fibre from the corresponding target. In a later paper, we will present the results of producing approximate flux-calibrated spectra from the data using the white dwarf targets we include where possible in the SDSS fields (see Sec. 4.5) and/or the optical photometry.

Significant refinement and further optimization of the 2DFDR code has been undertaken by one of us (SMC) and we have used these new versions of the software to have the most reliable, efficient reductions possible for our observing runs. Laplace filter cosmic ray rejection, Gaussian

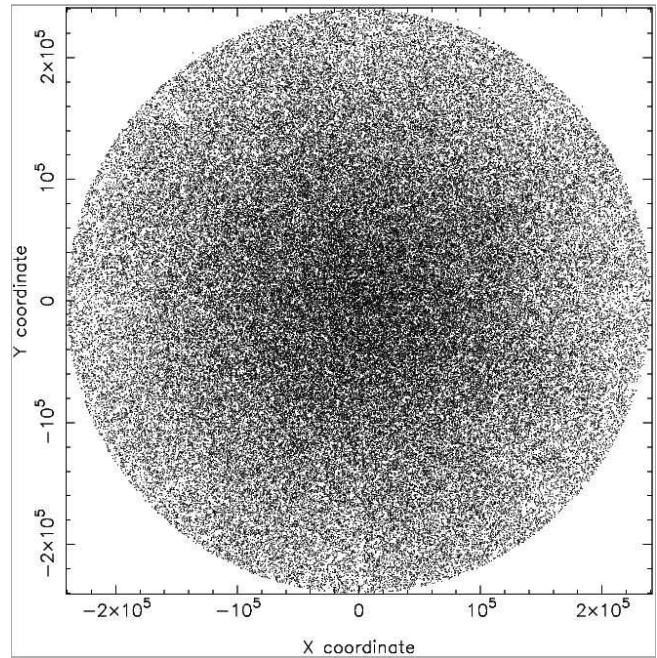


**Figure 10.** The average distribution of fibres observed on the two 2dF field plates. Each dot represents one fibre observed in the first two years of the project excluding 2007 April–August when we only observed inside the central 0.7 degree radius. The smooth distribution (apart from very small regions at the edge due to the eight guide fibre bundles) demonstrates that no artificial spatial signal is introduced by the observing process.

spectral extraction, 1D scattered light filtering and optimal sky subtraction have generally been used throughout the 2DFDR reductions (see Croom et al. 2005, for more details). Once the reduced, spliced file is generated for a field, as a final reduction step we apply a principal component analysis (PCA) sky subtraction algorithm to the spectra. This provides for better removal of the OH sky line contamination at the red end of the spectra, thus making it easier to identify redshifts. The PCA code we use was adapted (by KG and EW) from software developed by Wild & Hewett (2005). Our standard approach for implementing the PCA sky subtraction is to generate an eigenspectra file from the first 8–10 fields obtained on an observing run. This eigenspectra file is then used to PCA sky subtract the rest of the spectra obtained for a given run. We have found the PCA sky subtraction is a useful step in that it makes the redshifting a less onerous task by cleaning up the “cosmetics” of the spectra, particularly for data taken in good observing conditions.

## 5 REDSHIFT ANALYSIS

In this section we describe the process of redshift measurement from our spectroscopic data, as well as various tests of the reliability of these measurements.

### 5.1 Measurement

All redshifts in the WiggleZ survey are measured using an evolved version of RUNZ — the software used for both 2dF-

GRS (Colless et al. 2001) and 2SLAQ (Cannon et al. 2006). The original version of RUNZ made use of both discrete emission line redshift determination and absorption line redshifts via template Fourier cross-correlation (Tonry & Davis 1979). In the WiggleZ survey, it is rarely possible to make use of absorption lines—the survey is predicated on the ability to determine redshifts from emission lines alone. Therefore, RUNZ has been modified significantly (by SMC), optimizing it to measure redshifts from emission lines. The emission line algorithm searches for sharp peaks in the spectrum, as candidate emission lines, and then tries to match sets of these to known combinations of strong lines at different redshifts. The lines used are: [OII] $\lambda$ 3727, H $\beta$ , [OIII] $\lambda$ 4959, [OIII] $\lambda$ 5007, H $\alpha$ , and [NII] $\lambda$ 6583. We note that the adopted wavelength for the [OII] $\lambda$ 3727 doublet is not the mid-point of the two transitions (which is 3727.42Å), but rather is  $\sim 0.4$ Å redder to allow for the average ratio found in our spectra. For the cross-correlation measurement, RUNZ uses a revised set of template spectra including high-redshift galaxies and QSOs, but the continuum level in typical spectra is so low that the cross-correlation redshifts are very rarely used.

Uncertainties in the redshift measurements are estimated in two different ways by RUNZ. In the more common case when the redshifts are measured from emission lines, the redshifts are determined for each individual line by fitting Gaussian profiles, using the variance spectrum to determine the fitting errors. The final emission line redshift (and error) is the variance-weighted mean of that derived from the individual lines. For cross-correlation redshifts the error is derived from the width of the cross-correlation peak (Tonry & Davis 1979).

In practice, complete automation of the redshift measurements has proven to be problematic due to the noisy nature of many of the spectra and the presence of artifacts such as residuals from imperfect cosmic ray and sky removal and fibre fringing and cross-talk. After a redshift has been assigned using emission lines or the method of Tonry & Davis (1979), RUNZ automatically generates an integer quality flag ( $Q$ ) in the range 1–5 based on how well the template fits to the given spectra. The user then inspects the given redshift. In many cases, the user manually re-fits the spectrum and assigns a new redshift and quality flag, in accordance with the criteria in Table 10. In acknowledging that the assignment of  $Q$  values varies between users, we note that in any future analysis only redshifts with values of  $Q \geq 3$  will be utilized. Therefore, whilst there may be some debate as to what constitutes the difference between  $Q = 4$  and  $Q = 5$ , the critical separation in quality occurs between  $Q = 2$  and  $Q = 3$ . This can be seen in Figure 11 which displays redshift histograms for both  $Q \leq 2$  and  $Q = 3$  redshifts for data collected up until 2008 March. For the  $Q = 2$  redshift distribution, we see that there are multiple peaks that coincide with assigning [OII] to sky lines—such peaks are (with two exceptions) not present in the  $Q = 3$  distribution. Inspection of the two narrow peaks still visible in the  $Q = 3$  data shows that the first ( $z = 0.707$ ) corresponds to mis-matching [OII] to the weak sky line at 636.2 nm. The second peak ( $z = 0.761$ ) corresponds to mis-matching [OII] to rest-wavelength Galactic H $\alpha$  emission at 656.3 nm which occurs in a few fields. The number of spectra in these two peaks is less than 0.1 per cent of the total sample.

We present examples of a variety of WiggleZ spectra in

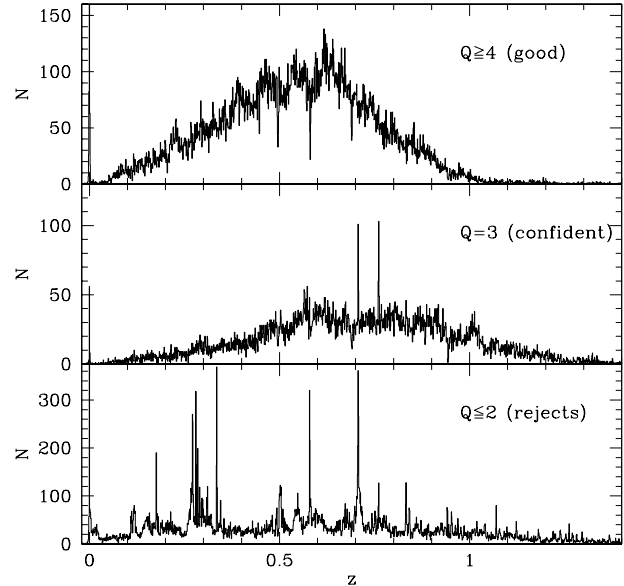


**Figure 11.** Redshift distribution as a function of the quality flag  $Q$ . The top two panels are for accepted measurements ( $Q$  of 3 and above). These show that objects at higher redshifts (with the H- $\beta$  line not visible) are generally not assigned the highest quality flags. The bottom panel is for rejected measurements ( $Q \leq 2$ ): this has many sharp peaks in the distribution corresponding to misidentified sky lines. With two exceptions (see text), these sharp peaks are not evident in the good ( $Q \geq 3$ ) redshift distributions.

**Table 10.** Redshift Quality Definitions

$Q$	%	Definition
1	21	No redshift was possible; highly noisy spectra.
2	19	An uncertain redshift was assigned.
3	18	A reasonably confident redshift; if based on [OII] alone, then the doublet is resolved or partially resolved.
4	33	A redshift that has multiple (obvious) emission lines all in agreement.
5	9	An excellent redshift with high S/N that may be suitable as a template.
6	0.5	Reserved for Galactic stars used as calibration sources.

Note: the second column lists the percentage of all observations (including repeats) in each category.

Figure 12 (high quality  $Q=4-5$ ), and Figure 13 (low quality  $Q=3$ ). The spectra include examples of those providing single [OII] doublet redshifts and standard multiple emission line detections. In Figure 14 we also present a random selection of QSO and star spectra from the survey. This demonstrates the relatively low redshifts of the few QSOs selected in the survey; many are only identified from the MgII emission line.

## 5.2 Redshift Reliability

The one hour exposures that the WiggleZ survey uses are too short to allow any significant detection of the continuum, with a continuum S/N  $\sim 1$  per (approx 0.14 nm) pixel.

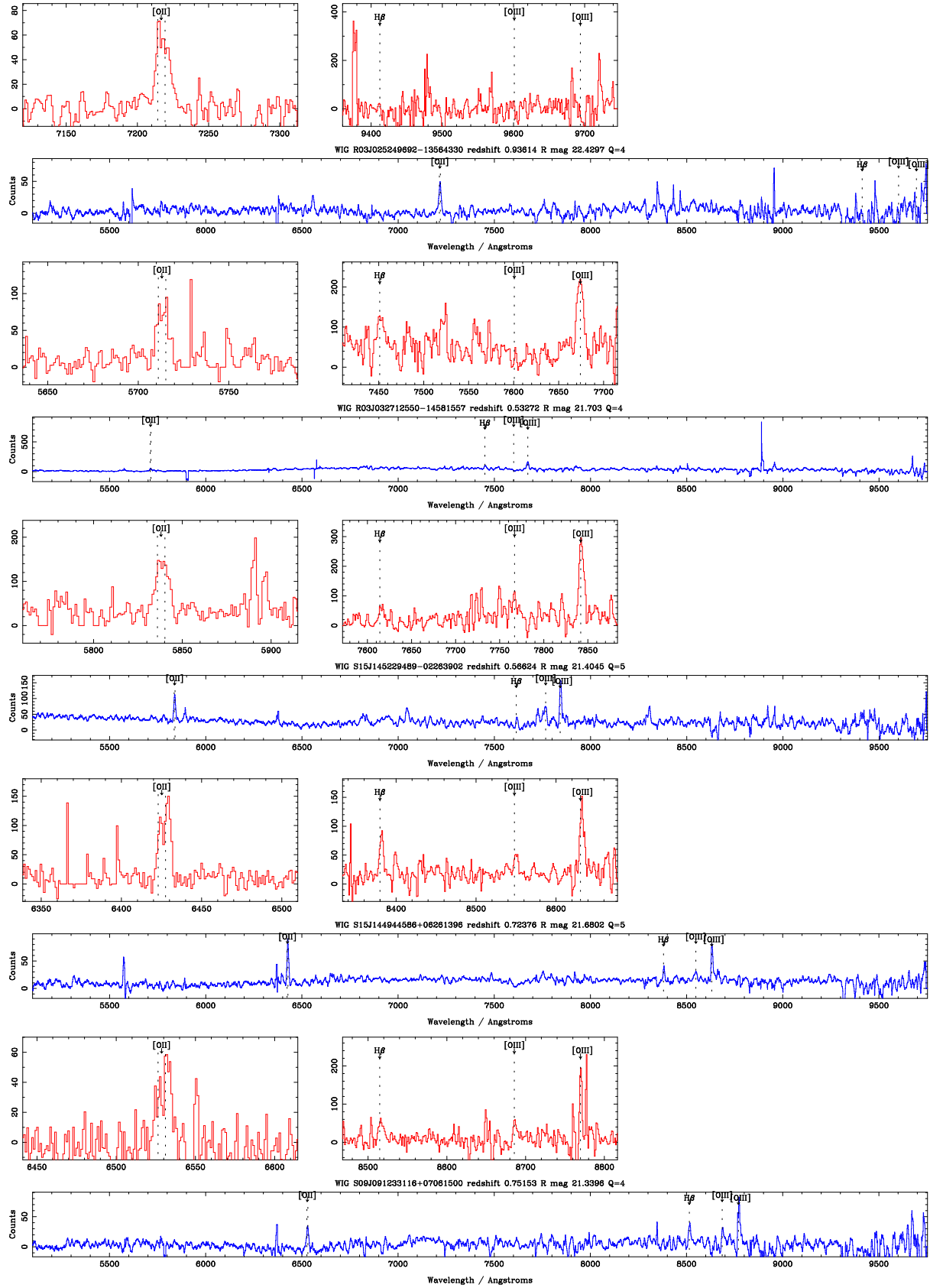


**Figure 12.** Examples of randomly-selected high-quality ( $Q=4,5$ ) spectra from the survey. For each spectrum, the upper panels (red) show the unsmoothed spectra zoomed in on the major emission lines, and the lower panel (blue) shows the whole spectrum, heavily smoothed in an optimal fashion.



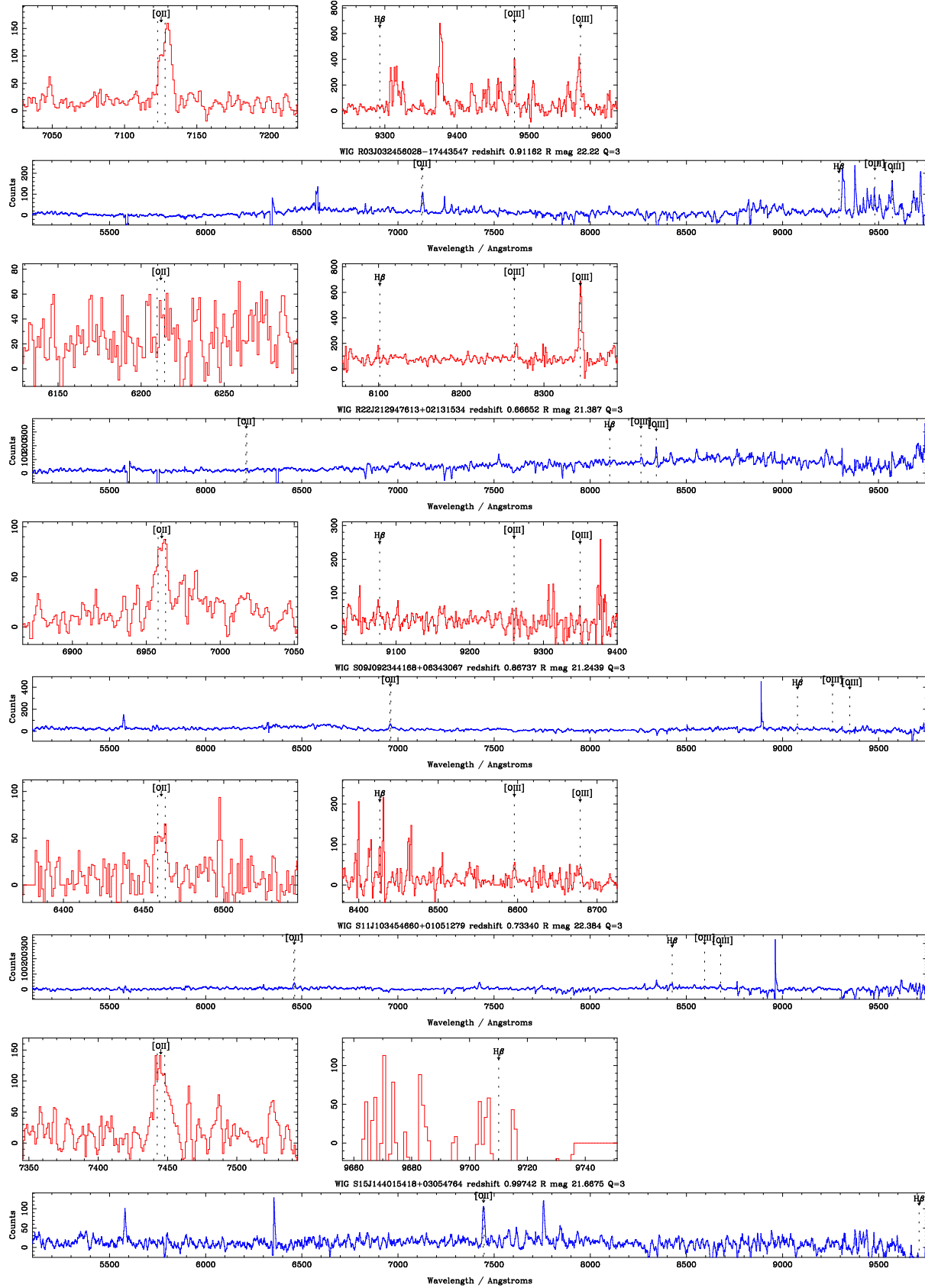


**Figure 13.** Examples of randomly-selected low-quality ( $Q=3$ ) spectra from the survey. For each spectrum, the upper panels (red) show the unsmoothed spectra zoomed in on the major emission lines, and the lower panel (blue) shows the whole spectrum, heavily smoothed in an optimal fashion.

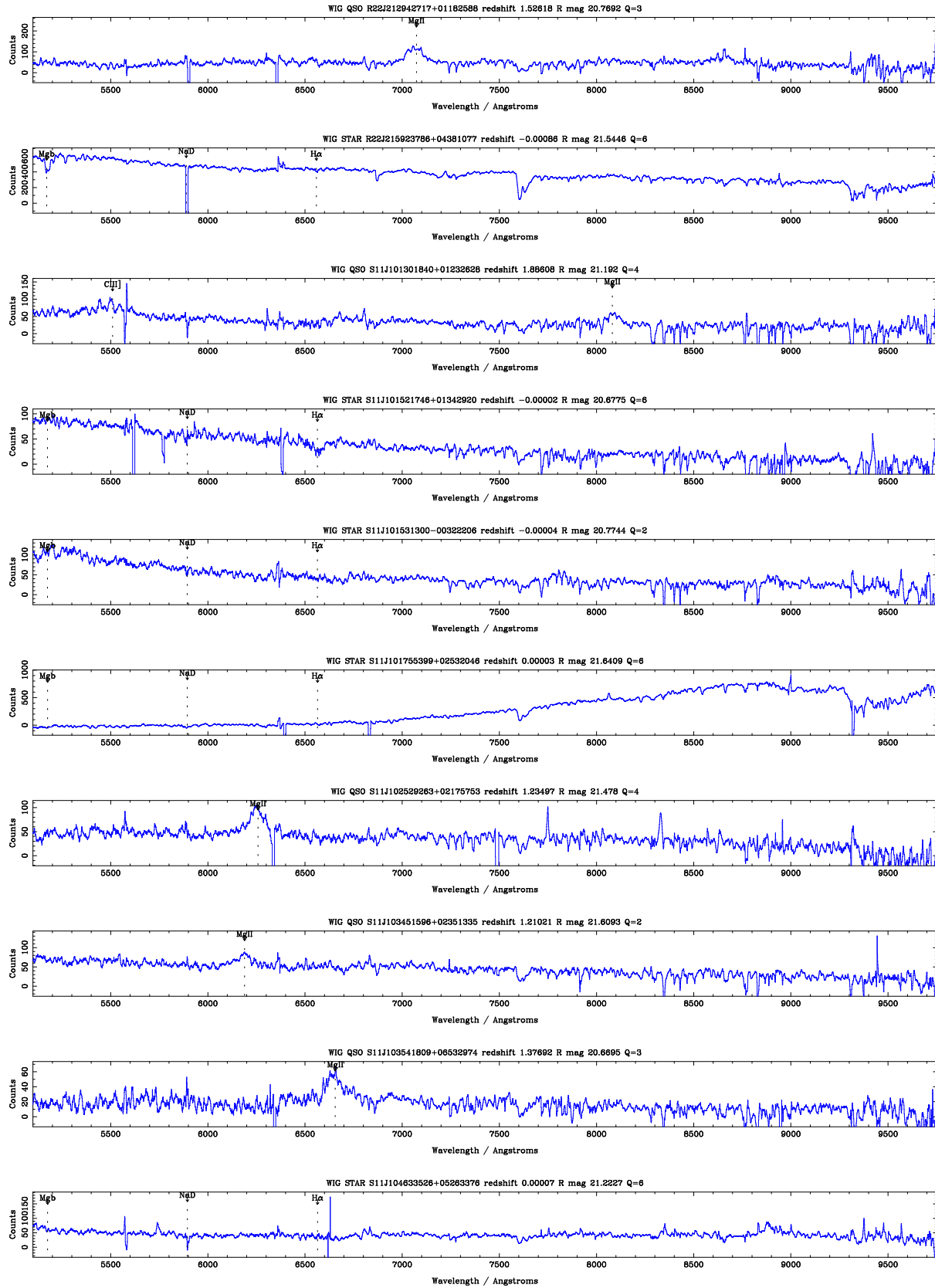


Figure 14. Examples of randomly-selected QSO and star spectra from the survey. For each object the whole spectrum is shown, heavily smoothed in an optimal fashion.

However, by design, we are able to reliably and accurately measure redshifts from the multiple bright emission lines in the WiggleZ galaxies. We commonly detect the [OII] $\lambda$ 3727, H $\beta$ , and [OIII] $\lambda$ 4959, 5007 emission lines in the spectra. At low redshifts ( $z < 0.26$ ), when the [OII] line moves outside of our wavelength range this is compensated by the ability to detect H $\alpha$  in our spectra. At higher redshifts ( $z > 0.95$ ) we often rely on redshifts obtained from a single line; however, the spectral resolution is sufficient to see this line significantly broadened at these redshifts (the [OII] doublet is often resolved at  $z \geq 0.8$ ) which allows us to confidently conclude this single line is [OII] and obtain the corresponding redshift. The reliability and accuracy of using the broadening to confirm a single line in a spectrum as the [OII] line of a high redshift emission line galaxy have already been demonstrated by van Breukelen et al. (2007).

### 5.2.1 Internal Tests

We have multiple  $Q \geq 3$  redshift measurements for over 6800 of the galaxies observed to date, for both the SDSS and RCS2 regions. These multiple ‘‘correct’’ redshift measurements can be used to estimate the accuracy of our redshift measurements, and assess the effectiveness of our redshift quality scheme. For the following analysis we define redshifts to be reliable (i.e. the correct lines have been identified) if they agree within  $|\Delta z| < 0.002$ . When converting to velocity differences, we calculate these according to  $\Delta v = c\Delta z/(1+z)$ .

We start by assessing the internal agreement within each of the three acceptable quality categories,  $Q = 3-5$ , by taking objects whose original and repeated measurements both have the same  $Q$  value. There are 737  $Q = 3$  repeats, 2263  $Q = 4$  repeats, and 619  $Q = 5$  repeats. The fractions of the redshift pairs that agree within each category are 68.5, 95.1, and 100 percent respectively. For the correctly identified redshifts, the mean difference is not significantly different from zero in any of the categories, and the standard deviations are  $\sigma_{\Delta z Q=3} = 0.0042$  (68.5 km s $^{-1}$ ),  $\sigma_{\Delta z Q=4} = 0.0031$  (58.2 km s $^{-1}$ ), and  $\sigma_{\Delta z Q=5} = 0.0022$  (41.6 km s $^{-1}$ ) respectively. (These values are for the differences of two measurements so the uncertainty in an individual measurement would be a factor of  $\sqrt{2}$  times smaller.) As expected, and as shown in Fig. 15 the scatter in the redshift differences decrease with increasing  $Q$ .

Given the high reliability of the  $Q = 4, 5$  measurements, we can now test a larger sample of  $Q = 3$  objects for which the repeated measurement has a higher quality ( $Q \geq 4$ ) and can therefore be regarded as correct. There are 2250 such objects, of which 78.7 per cent are correct; the standard deviation in the redshift differences is  $\sigma_{z Q=3-4/5} = 0.0039$  (67.5 km s $^{-1}$ ). The fraction of reliable measurements is consistent with the internal value (68.5 per cent) reported above. Similarly, 1425  $Q = 4$  objects are repeated by higher  $Q = 5$  measurements, of which 98.3 are correct and  $\sigma_{z Q=4-5} = 0.0029$  (54.0 km s $^{-1}$ ). The average reliability and uncertainty values for the three quality categories are summarised in Table 11. These values are consistent with earlier estimates made by Blake et al. (2009a) for a subset of the current data.

The comparisons of the repeat observations may also be used to check the internal redshift uncertainties  $\sigma_{z, runz}$  for each measurement estimated by the RUNZ code. Those inter-

**Table 11.** Reliability and Uncertainty of Redshift Measurements

Quality $Q$	Reliability	Uncertainty	
		$\sigma_z$	$\sigma_v$ (km s $^{-1}$ )
3	78.7 %	0.00030	48.4
4	98.3 %	0.00022	41.2
5	100.0 %	0.00016	29.4

Notes: the reliability fractions were obtained by comparing with repeated measurements at higher quality ( $Q$ ) values. The measurement uncertainties  $\sigma_z, \sigma_v$  were obtained by scaling the internal standard deviations by  $1/\sqrt{2}$ . The velocity differences for each measurement were calculated as  $\Delta v = c\Delta z/(1+z)$ .

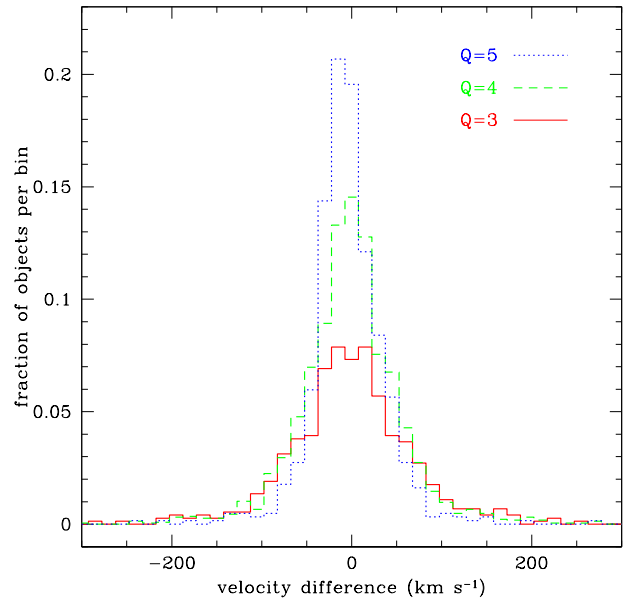


**Figure 15.** Redshift differences from repeat observations of WiggleZ targets. The three histograms show the distribution of redshift differences in pairs of repeated WiggleZ observations. The solid, dashed and dotted curves are for pairs in which the qualities of the both measurements are 3, 4, and 5 respectively.

nal uncertainties have a median value of  $\sigma_{z, runz} \approx 0.00015$  for all three quality bins combined, but the distribution is very non-uniform, with a long tail to higher values. Considering just this median estimate of  $\sigma_z = 0.00015$ , we find that it corresponds well to the  $\sigma_z = 0.00016$  derived for the  $Q = 5$  measurements in Table 11. The empirical results for the  $Q = 3, 4$  uncertainties in the table are larger than this, so in these cases the internal redshift uncertainty may be an underestimate.

We also examined the redshift differences as a function of redshift, for all galaxies with multiple  $Q \geq 3$  redshift measurements. We do not find any systematic variation with redshift of the mean or standard deviation of the differences. We conclude that the redshift uncertainties quoted above are valid over the entire redshift range of the WiggleZ survey. This is, however, a trend in the reliability of the  $Q = 3$  redshift measurements: the reliability decreases from about 80 per cent to about 40 per cent between redshifts of  $z = 0.8$  and  $z = 1.2$  (see Fig. 6 of Blake et al. 2009a).

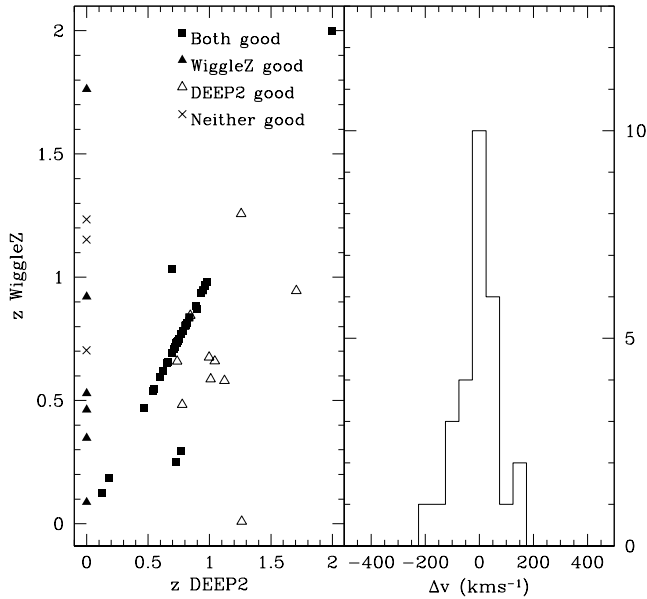


**Figure 16.** Comparison of WiggleZ redshifts with DEEP2 survey data. The left-hand panel compares the different redshifts with the symbols indicating the reliability status of the measurements in the respective surveys. The right-hand panel shows the histogram of redshift differences.

### 5.2.2 External Tests

At the time of writing, there are very few other galaxy surveys in our redshift range that overlap with the WiggleZ survey, so there are few opportunities for external comparison. There is a small overlap between WiggleZ and Data Release 3 of the DEEP2 survey (Davis et al. 2003) in our 22-hour field. Although the DEEP2 survey (in that region) is aimed at  $z > 0.5$  targets, there are 53 sources in common with WiggleZ (positions matching to within 2.5 arc seconds). The estimated r.m.s. uncertainty in the DEEP2 redshifts is  $30 \text{ km s}^{-1}$  with less than 5 per cent incorrectly identified (Davis et al. 2003).

We compare the WiggleZ and DEEP2 redshifts in Fig. 16. Of the 34 sources that both surveys assign good redshifts to, only 3 disagree substantially (due to different line identifications). Of the redshifts that disagree, all three are  $Q = 3$  WiggleZ measurements; no  $Q = 4$  or 5 WiggleZ measurements disagree with the DEEP2 measurements. On careful inspection of the WiggleZ spectra and the corresponding DEEP2 spectra we conclude that in two cases the DEEP2 value is correct; the third case is ambiguous so we cannot determine which is correct. This rate of misidentification among the  $Q = 3$  WiggleZ redshifts (20-30% of the  $Q = 3$  redshifts are wrong) is entirely consistent with the internal estimates in Section 5.2.1 above.

Restricting the sample to those that agree within  $|\Delta z| < 0.002$ , there is no significant mean difference ( $\overline{\Delta z} = -0.00003 \pm 0.00002$ ) and the rms difference is  $\sigma_{\Delta z} = 0.00047$  ( $80.5 \text{ km s}^{-1}$ ). This scatter is entirely consistent with the estimates of the internal uncertainties in the respective surveys quoted above.

## 6 INITIAL RESULTS

The primary aim of our project — measurement of the baryon acoustic oscillation scale — cannot be completed without the full data set. However there are many secondary scientific projects possible with the data currently available. In this section we describe some initial results from the current data sample. We focus on the properties of the measured galaxies, noting in particular the success of our methodology in selecting high-redshift galaxies.

### 6.1 Success of Target Selection

The whole WiggleZ survey strategy is based on the ability to select high-redshift emission-line galaxies for the spectroscopic observations. We initially selected galaxies based on the UV and UV-optical colours, but then improved the selection with optical colour selection to remove some of the low-redshift targets as described in Section 3.5. The success of this strategy is demonstrated in Figure 7 by an increased fraction of high-redshift targets in both the SDSS and RCS2 regions. In the SDSS fields the median redshift increases from  $z_{med} = 0.53$  to  $z_{med} = 0.61$ . In the RCS2 fields, the more accurate optical colours permit a greater improvement: the median redshift increases from  $z_{med} = 0.54$  to  $z_{med} = 0.67$ . In the combined sample the median redshift is  $z_{med} = 0.63$  and the redshift range containing 90 per cent of the galaxies is  $0.22 < z < 1.02$ .

The ability of the survey to obtain the required number of galaxies is also a function of the spectroscopic *success rate*, defined as the fraction of observations for which we obtain a reliable ( $Q \geq 3$ ) redshift. By comparison, the overall survey *completeness* is defined as the fraction of all the input targets for which we obtain a reliable ( $Q \geq 3$ ) redshift.

The mean spectroscopic success rate for the survey so far is 60 per cent (Table 1); the completeness (after the repeated observations) is 70 per cent. Longer exposures would enable a higher success rate and better quality spectra but would result in greatly diminished values for the total area and total number of galaxies covered and hence a poorer BAO measurement.

The main factor that strongly affects the success rate is the weather: it drops by around 20 per cent when observations are taken through cloud. (In the first half of the survey, 57 per cent of the allocated time was clear and we observed through cloud for an additional 9 per cent of the time.) In Figure 17 we show that the success rate is not a strong function of the continuum  $r$  magnitude. This is expected as we are measuring the redshifts from emission lines and not from continuum features. The upper panel of Fig. 17 shows the distribution of  $r$  magnitudes for the targets: this shows steps at half-magnitude intervals due to our prioritization scheme (see Table 5).

### 6.2 Galaxy Properties

We will examine the physical properties of the WiggleZ galaxies in detail in later papers, but some preliminary observations can be made at this stage.

The WiggleZ galaxy sample clearly favours blue galaxies with strong emission lines as a result of the primary NUV flux limit and the  $NUV - r$  colour selection. This selection

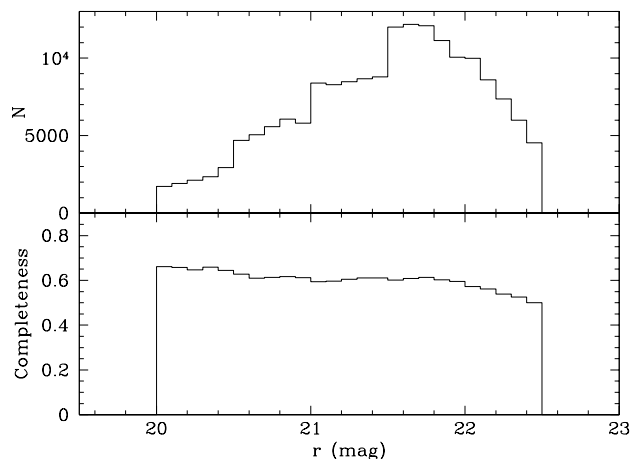


**Figure 17.** Spectroscopic success rate of the WiggleZ survey as a function of  $r$  magnitude. Top: the  $r$ -magnitude distribution of the observed targets. The steps are caused by our prioritisation scheme (see Table 5). Bottom: success rate defined as the fraction of observed targets for which good redshifts were measured, shown as a function of  $r$  magnitude.

has been quantified by our analysis of DEEP2 (Davis et al. 2003) galaxies for which deep optical and GALEX observations were available. (see Section 3.5). We find that, as expected, the WiggleZ targets are blue compared to optically-selected galaxies: 82 (99) per cent of the WiggleZ targets are bluer than  $B - R = 1.2$  (1.8).

We have investigated the physical morphology of the WiggleZ galaxies by searching the *Hubble Space Telescope* archive for any images that are available of the WiggleZ galaxies we have observed. We present a selection of these images in Figure 18. The images show that a very large fraction of the WiggleZ galaxies are interacting or show other signs of a disturbed morphology. This suggests that merger activity may play an important role in driving the strong star formation detected in the WiggleZ galaxies. In terms of the galaxy photometry, we also note that about 25 per cent of the images reveal more than one galaxy within the  $\approx 4$  arc second PSF of GALEX. In these cases the UV photometry may include both sources whereas the optical measurements may include only one of the sources.

The most direct physical measurement we have for each WiggleZ galaxy is from the various emission lines in the spectra, notably [OII] which is the one line present in nearly all spectra. At low redshifts ( $z \lesssim 0.35$  for the old dichroic and  $z \lesssim 0.48$  for the new dichroic), both  $H\beta$  and  $H\alpha$  are also visible. This is below the median redshift range for the survey, but it does provide a sub-sample of galaxies for which we can investigate the line diagnostics. In Fig. 19 we show the “BPT” (Baldwin, Phillips, & Terlevich 1981) line ratio diagnostic plot for low-redshift galaxies in our sample. Note that the two lines in each ratio ([OIII]/ $H\beta$  and [NII]/ $H\alpha$ ) are at very similar wavelengths, so the plot can be constructed from spectra that have not been flux calibrated. We also show in the figure the “maximal star formation” boundary line (Kewley et al. 2001) between the star formation (below the line) and the active galaxy (above the line) domains. The plot shows most (90 per cent) of the WiggleZ galaxies

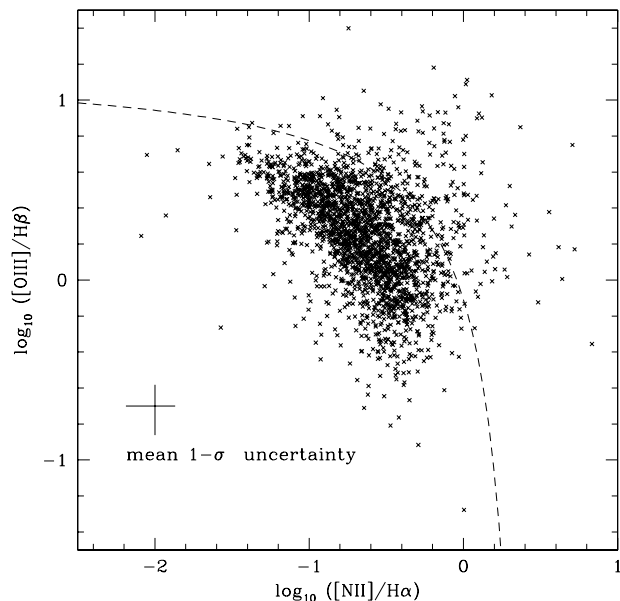


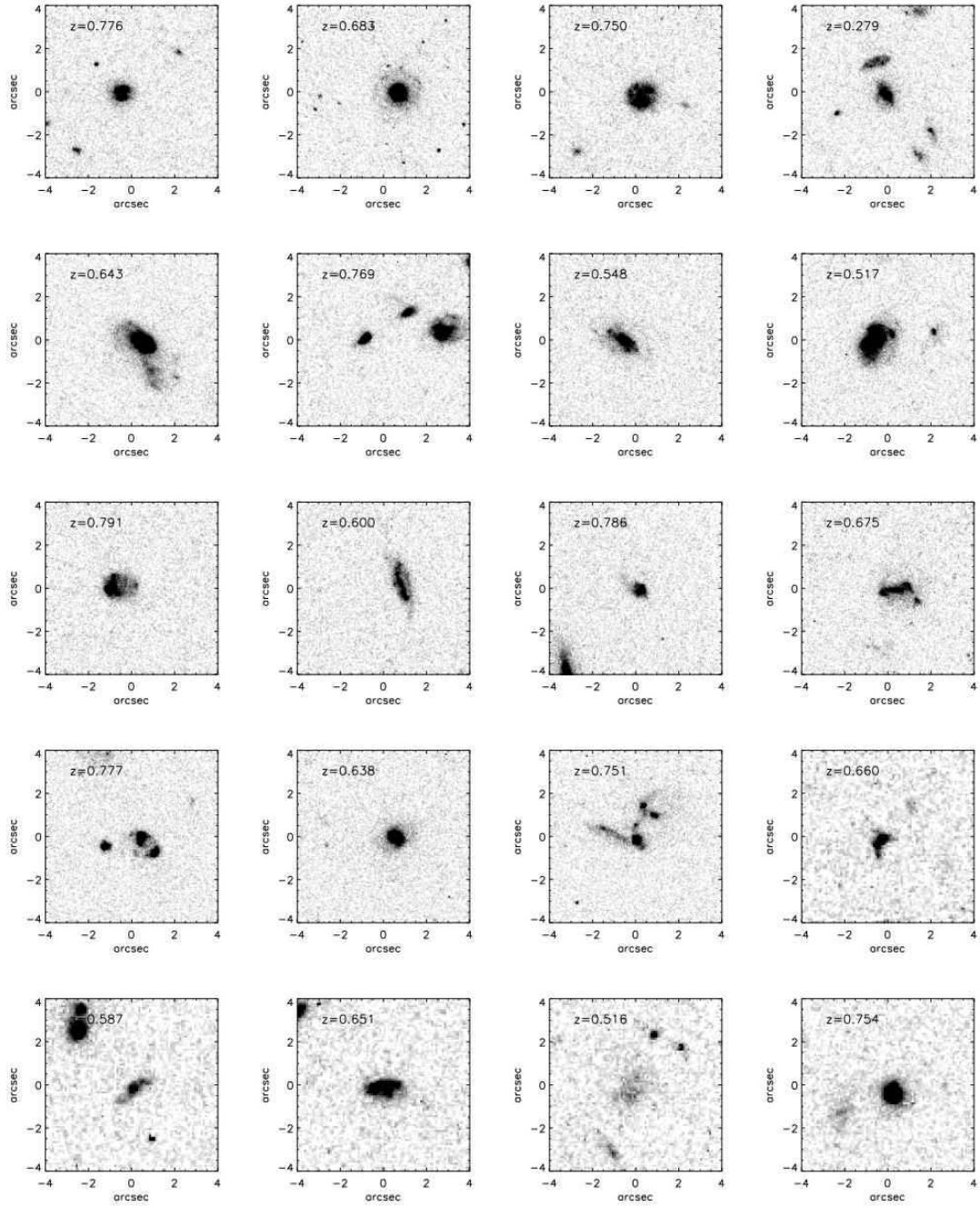
**Figure 19.** Emission line ratios of WiggleZ galaxies. In this “diagnostic” plot the dashed line indicates the Kewley et al. (2001) extreme star formation envelope. Any galaxies above the dashed line are dominated by AGN activity and not star formation. The diagram shows that the WiggleZ galaxies are predominantly star-forming galaxies. The plot is based on a low-redshift subset of the WiggleZ sample because we cannot measure [NII] and  $H\alpha$  emission at redshifts above  $z \approx 0.4$ .

fall below the nominal boundary line, confirming that we are mainly selecting star-forming galaxies as intended.

We can also use the [OIII]/ $H\beta$  line ratio to show that the higher redshift targets are not dominated by AGN. In Figure 20 we compare the distributions of the [OIII]/ $H\beta$  line ratio for galaxies above and below a redshift of  $z = 0.45$ . It is clear from the figure that the high redshift galaxies do not have any large excess with high line ratios, indicative of AGN. In the low redshift sample that we analysed in Figure 19, the fraction with  $\log_{10}[\text{OIII}]/H\beta > 0.9$  is 1 per cent, compared to 2 per cent for the galaxies at higher redshifts ( $z > 0.45$ ).

### 6.3 Galaxy Distributions

We show an example of the spatial distribution of the WiggleZ galaxies from the 15-hour field as cone plots projected onto the Right Ascension plane in Figure 21. The large-scale radial features in the plots are due to the incomplete coverage of the survey at present. In the remaining regions of the plots, especially the lower plot, some evidence of spatial clustering is revealed by visual inspection. This is in contrast to similar plots for the 2dF Galaxy Redshift Survey (Colless et al. 2001) and the 2SLAQ Luminous Redshift Galaxy Survey (Cannon et al. 2006), both of which show strong evidence of clustering in similar diagrams. This difference is expected because the WiggleZ galaxies are comparatively rarer objects with much larger median separations than the other samples. Furthermore, we are surveying much larger spatial scales. The distribution of WiggleZ galaxies

Figure 18. High-resolution *Hubble Space Telescope* archive images of a selection of WiggleZ galaxies. Each image is 8 arc seconds on a

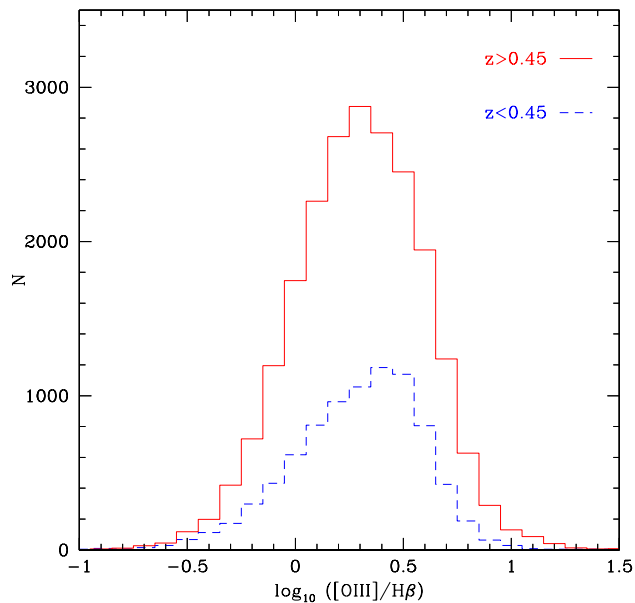


**Figure 20.** A comparison of the [OIII]/H- $\beta$  line ratios of high ( $z > 0.45$ ) and low ( $z < 0.45$ ) redshift WiggleZ galaxies. Analysis of the low-redshift sample (Fig. 19) shows that it does not contain large numbers of AGN. This figure shows that the high redshift sample does not contain any large excess of AGN, as would be indicated by line ratios of  $\log_{10}[\text{OIII}]/\text{H}\beta > 0.9$ .

probes clustering on 100 Mpc scales where it is weaker than on the much smaller scales probed by, for example, the 2dFGRS.

### 6.3.1 Small-scale galaxy clustering

Although the WiggleZ galaxies are not as strongly clustered as red galaxies, their intrinsic small-scale clustering strength is a crucial design parameter for the main WiggleZ survey. We have used the early survey data to measure this small scale clustering. We find that the clustering is actually much stronger than that measured previously for UV-selected galaxies at low redshifts ( $z \approx 0$ ). We measure a clustering length of  $r_0 = 4.40 \pm 0.12 h^{-1}$  Mpc (Blake et al. 2009a). This is comparable to the Lyman break galaxies measured in high redshift ( $z \approx 3$ ) surveys; the combined flux limits and colour selection of the WiggleZ survey are selecting extremely luminous blue galaxies that are relatively strongly clustered. This is highly advantageous for our survey design, as discussed above.

We have estimated the final precision of the survey in measuring the dark energy equation of state parameter  $w$  assuming a model with constant  $w$  (Blake et al. 2009a). We include the 5-year WMAP cosmic microwave background data (Komatsu et al. 2009) and the latest supernova data from the SNLS, *HST* and ESSENCE projects (Astier et al. 2006; Riess et al. 2007; Wood-Vasey et al. 2007) to predict marginalised errors in our model of  $\sigma(\Omega_m) = 0.02$  and  $\sigma(w_{const}) = 0.07$ . Not only is this more precise than previous estimates, but the method is independent and eliminates existing degeneracy in the  $(\Omega_m, w_{const})$  plane (see Fig. 20 of Blake et al. 2009a).

### 6.3.2 The Galaxy Power Spectrum

We have also measured the three-dimensional power spectrum of the WiggleZ galaxies on large scales. We find that a model power spectrum based on linear theory is a good fit to the data over a wide range of scales up to a maximum wave number of  $k < 0.25 h \text{ Mpc}^{-1}$  (Blake et al. 2009b). The fit extends to such large wave numbers because of the high redshifts of the WiggleZ galaxies and their relatively low bias. We also detect the imprint of peculiar velocities when comparing the power spectrum measurements as a function of radial and tangential wave numbers: the results are consistent with a redshift space distortion parameter of  $\beta = 0.5$ .

## 7 FIRST PUBLIC DATA RELEASE

This paper accompanies the first public data release from the WiggleZ survey, made at the half-way point in terms of allocated observing nights. In this section we summarise the current status of the survey and give details of the survey database design and the first public data release.

### 7.1 Survey Progress

At the end of the 2008A observing semester, the WiggleZ Survey reached its half-way point in terms of scheduled nights on the telescope (see Table 7): 112 of a nominal 220 nights had been scheduled. Several improvements were made to the survey design parameters in the first twelve months as a result of the initial observations, but the design and performance are now stable.

The key parameters of the survey performance are summarised in Table 1. The first part of the table lists the various parameters we obtain for the survey which, when multiplied together give us the rate of galaxies successfully observed per clear night. In the second half of the table we calculate the length of the survey needed in order to observe the 240,000 galaxies we need for the clustering measurements. This comes to about 160 clear nights, corresponding to 220 nights when we include the standard factor of 1.33 to allow for bad weather.

As noted above, the total number of survey galaxies required to be observed is a function of the target selection and the observational success rate. Other factors such as the number of fibres allocated per field and the number of fields observed per night also enter into the calculation which is summarised in Table 1. In Fig. 22 we present the actual results of the observations graphically, showing the cumulative number of survey galaxies successfully observed as a function of the number of clear nights used. This is compared to the required rate of 1442 survey galaxies per clear night to reach 240,000 galaxies in the full survey. As can be seen from the figure, the survey is almost on schedule to achieve this goal.

### 7.2 Database design and web application

The WiggleZ Survey is a complex, multi-year campaign involving the collection of many nights of observational data. Thus a sophisticated, reliable data archiving system is an absolute necessity. Our general approach is to take the raw and

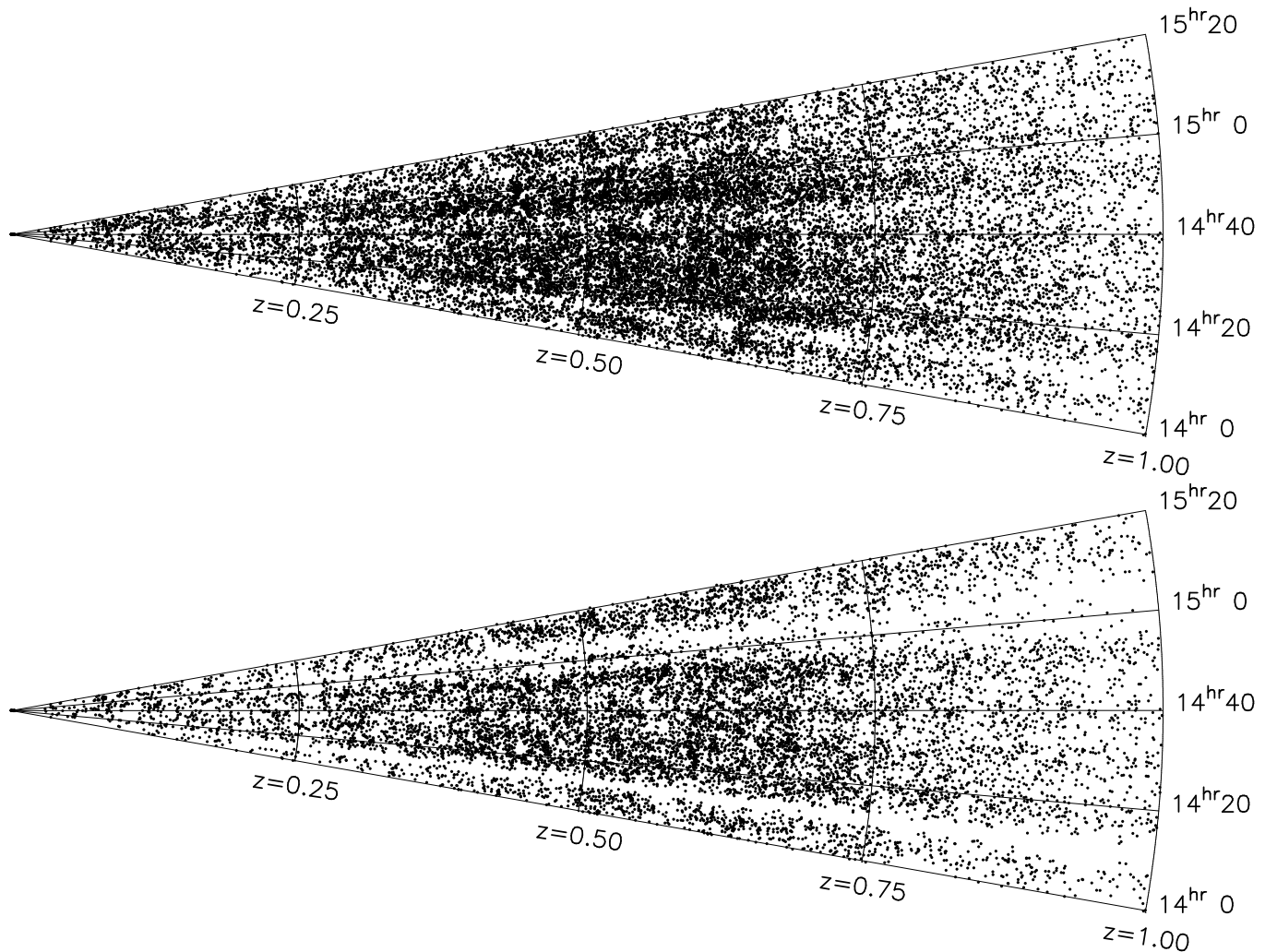


**Figure 21.** The spatial distribution of WiggleZ galaxies observed in the 15-hour region. Each plot shows the comoving positions of the galaxies projected onto Right Ascension. The full width shown — the comoving distance to a redshift of  $z = 1$  — is 3.3 Gpc. The upper plot shows all galaxies in the field. The lower plot only includes galaxies with Declinations greater than +1 degree (about half the sample) to make the small scale clustering easier to discern.

reduced data, observational logs, catalogue and other associated files and organize them within a well defined directory structure on a large cluster server. An extensive suite of software has been developed (by NJ) to serve the data from this archive via a MySQL database and “Ruby on Rails” web application. Python scripts have also been built to assist in the data uploading, checking and management of the archive.

The web application gives access to data subsets using a simple search interface which allows queries based on the observation dates, target identifiers, regions in the sky, filter bandpasses, redshift range and other parameters, or some combination thereof. All these parameters for the large number of targets have been captured in the database. Users can also execute more complex, custom SQL queries on the database via the web application. Catalogues of targets, and the associated FITS files of the reduced spectra, can be downloaded for analysis. Finally, users of the web application can also upload catalogues of objects to be cross-matched against targets currently residing in the WiggleZ data archive.

The WiggleZ web application and database have been designed to capture all the pertinent data regarding the observations so that we can analyze our large data set with as many approaches as possible, thus maximizing the scientific return. The web application is very user-friendly and well documented, such that a novice user can soon execute complex queries of the database with minimal training. A cookbook of possible web application uses is provided along with visual explanations of the various features. Since the web application has the flexibility of allowing both simple searches and more complex, custom SQL queries, users can mine the database for the specific results that they seek. After a successful query of the database the user can then use the search results page to: select and view an individual spectrum, select (sub-)sets of resultant targets for download as a tar file of FITS spectra files or as a catalog file (in ASCII, VOTable or FITS format). When viewing an individual spectrum from a search, the associated GALEX and optical images of the target (when either are available) are displayed, and the user has the capability of zooming in on



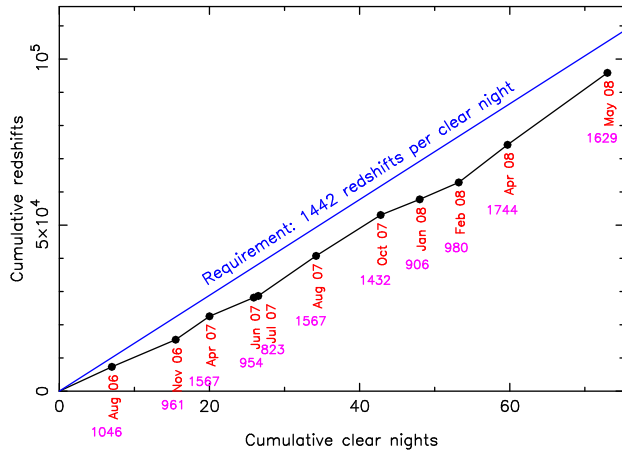


**Figure 22.** Overall progress of the WiggleZ survey measured by the number of galaxies with redshifts measured per clear night. The target number of 1442 galaxies per clear night is based on our overall target of 240,000 galaxies given the standard clear weather fraction of 0.75 and a survey duration of 220 nights. Data points are shown for each observing run, with the number of redshifts measured per clear night in each run printed below each point.

the spectrum, applying Gaussian smoothing and downloading hard copy files (in FITS or postscript format).

The web application also allows a user to upload a space-separated ASCII file containing RA and DEC positions of targets, to cross-match this list with targets in the WiggleZ database. The results of the cross-matching can be downloaded in the form of either ASCII, VOTable or FITS table catalogues, or as a tar file of FITS files containing the spectra. Finally, download requests of selected spectra or catalogues from the search results page results in the user being redirected to the “pending requests” page. On this web page, multiple queries by a user can be left pending and downloaded at a later time.

### 7.3 Public Database Release

The first public release of WiggleZ data (DR1) aims to provide the astronomical community with an opportunity to utilize our large data archive well before the survey is complete and before the final, complete data release. This first data release is available via the following URL: <http://wigglez.swin.edu.au/>. This web page does not require secure access and is available to any user who wants to access the DR1 data.

The WiggleZ DR1 database provides the target coordinates, photometry and redshifts, along with the quality of the determined redshifts, downloadable in ASCII, VOTable and FITS table format. It should be emphasized that the DR1 targets will also have their FITS spectra files publicly accessible via the website. We have included the UV and optical magnitudes for all of the targets in DR1, where available. The DR1 public data release includes all observations up to the end of Semester 2008A: a total of 169,000 spectra with 100,138 successful redshift measurements. The median redshift is  $z = 0.6$  and the redshift range containing 90 per cent of the galaxies is  $0.2 < z < 1.0$ .

## 8 SUMMARY

The WiggleZ Dark Energy Survey will be the first large-volume spectroscopic galaxy survey to measure the BAO scale in the key redshift range of  $0.2 < z < 1.0$ . In this paper we have described the design and initial results of the WiggleZ Survey at the half-way point which coincides with our first public data release.

To emphasise the large size of the WiggleZ survey we note that, as of 2008 December, we have measured 119,000 galaxy redshifts, of which 73 000 have redshifts  $z > 0.5$ . This means we have already more than doubled the number of known galaxy redshifts above  $z = 0.5$  from the two largest existing surveys: DEEP2 (Davis et al. 2003) with  $N_{z>0.5} \approx 28,000$  and the VIMOS VLT Deep Survey (VVDS, Garilli et al. 2008) with  $N_{z>0.5} \approx 18,000$ . At the time of writing, the total number of  $0.5 < z < 1.5$  redshifts published from all surveys is 100,000 (as listed by NED). The WiggleZ survey, when completed, will more than double this quantity.

Our survey design relies on the use of GALEX UV satellite data to efficiently select high-redshift emission line galaxies. These objects, whilst fainter than giant red galaxies at the same redshift, can be observed very efficiently on a 4-metre class telescope because of their strong emission lines. We have added some optical colour selection to our UV colour selection to further improve the fraction of galaxies with high redshifts; the median redshift of the measured galaxies is now  $z_{med} = 0.63$ . The high sensitivity of the new AAOmega spectrograph on the AAT and the short fibre configuration time of the 2dF positioner mean that we can observe a new field every 1.2 hours allowing us to make rapid progress on the survey.

In this paper we have also presented our first public data release, available from a dedicated web interface. The public data comprise photometry (optical and UV), redshifts and spectra of all objects observed up to the end of Semester 2008A.

We cannot make the BAO clustering measurement at this stage of the project. This is not only because we only have half the necessary sample but also because the window function is very irregular due to our highly variable coverage of the fields to date. However, at the half-way stage we already have the largest ever sample of high redshift emission line galaxy spectra. Most importantly, we have measured the small-scale clustering of these UV-luminous galaxies and found it to be relatively strong which increases the accuracy with which we will be able to measure the BAO scale. At lower redshifts where we can measure the  $H\beta$  line we have shown that the WiggleZ galaxies are mostly extreme starburst-type galaxies as expected. We have compared the WiggleZ galaxies to optically-selected galaxies at the same redshift and confirmed that they are extremely blue with high star formation rates. There is some evidence from *Hubble Space Telescope* imaging of a subset of the galaxies that the starburst activity is being driven by interactions.

## ACKNOWLEDGMENTS

This project would not be possible without the superb AAOmega/2dF facility provided by the Anglo-Australian

Observatory. We wish to thank all the AAO staff for their support, especially the night assistants, support astronomers and Russell Cannon (who greatly assisted with the quality control of the 2dF system).

We also wish to thank: Alejandro Dubrovsky for writing software used to check the guide star and blank sky positions; Maksym Bernyk and David Barnes for help with the database construction; Peter Jensen and Max Spolaor for assistance with the redshift measurements; Michael Stanley for help with the selection of new GALEX positions; and Michael Cooper for providing DEEP2 spectra for the comparison in Sec. 5.2.2.

We wish to acknowledge financial support from The Australian Research Council (grants DP0772084 and LX0881951 directly for the WiggleZ project, and grant LE0668442 for programming support), Swinburne University of Technology, The University of Queensland, the Anglo-Australian Observatory, and The Gregg Thompson Dark Energy Travel Fund.

GALEX (the Galaxy Evolution Explorer) is a NASA Small Explorer, launched in April 2003. We gratefully acknowledge NASA's support for construction, operation and science analysis for the GALEX mission, developed in co-operation with the Centre National d'Etudes Spatiales of France and the Korean Ministry of Science and Technology.

Funding for the SDSS and SDSS-II has been provided by the Alfred P. Sloan Foundation, the Participating Institutions, the National Science Foundation, the U.S. Department of Energy, the National Aeronautics and Space Administration, the Japanese Monbukagakusho, the Max Planck Society, and the Higher Education Funding Council for England. The SDSS Web Site is <http://www.sdss.org/>.

The RCS2 survey is based on observations obtained with MegaPrime/MegaCam, a joint project of CFHT and CEA/DAPNIA, at the Canada-France-Hawaii Telescope (CFHT) which is operated by the National Research Council (NRC) of Canada, the Institut National des Sciences de l'Univers (CNRS) of France, and the University of Hawaii. The RCS2 survey is supported by grants to H.K.C.Y from the Canada Research Chair program and the Discovery program of the Natural Science and Engineering Research Council of Canada.

## REFERENCES

- Adelman-McCarthy J. K., et al., 2006, *ApJS*, 162, 38  
 Astier P., et al., 2006, *A&A*, 447, 31  
 Baldwin J. A., Phillips M. M., Terlevich R., 1981, *PASP*, 93, 5  
 Becker R. H., White R. L., Helfand D. J., 1995, *ApJ*, 450, 559  
 Bennett C. L., et al., 2003, *ApJS*, 148, 1  
 Bertin E., Arnouts S., 1996, *A&AS*, 117, 393  
 Blake C., Glazebrook K., 2003, *ApJ*, 594, 665  
 Blake C., Parkinson D., Bassett B., Glazebrook K., Kunz M., Nichol R. C., 2006, *MNRAS*, 365, 255  
 Blake C., et al., 2009a, *MNRAS*, 395, 240  
 Blake C., et al., 2009b, *MNRAS*, submitted.  
 van Breukelen C., et al., 2007, *MNRAS*, 382, 971  
 Bruzual A. G., Charlot S., 1993, *ApJ*, 405, 538  
 Campbell L., Saunders W., Colless M. 2004, *MNRAS*, 350, 1467  
 Cannon R., et al. 2006, *MNRAS*, 372, 425  
 Cole S., et al., 2005, *MNRAS*, 362, 505  
 Coleman G. D., Wu C.-C., Weedman D. W., 1980, *ApJS*, 43, 393  
 Crook P., 1993, *MNRAS*, 262, 1065  
 Colless M., et al. 2001, *MNRAS*, 328, 1039  
 Cooray A., Hu W., Huterer D., Joffe M., 2001, *ApJ*, 557, L7  
 Croom, S., Saunders, W., Heald, R., and Bailey, J. 2005, "The 2dfdr Data Reduction System Users Manual (January 2005)", see <http://www.aao.gov.au/AAO/2df/aaomega/>  
 Davis M., et al., 2003, *SPIE*, 4834, 161  
 Eisenstein D., 2002, *ASPC*, 280, 35  
 Eisenstein D. J., et al., 2005, *ApJ*, 633, 560  
 Eisenstein D. J., et al., 2006, *AJ*, 132, 676  
 Efstathiou G., Sutherland W. J., Maddox S. J., 1990, *Natur*, 348, 705  
 Fioc M., Rocca-Volmerange B., 1997, *A&A*, 326, 950  
 Frieman, J.A., Turner, M.S., Huterer, D., 2008, *Ann. Rev. Astron. Astrophys.*, 46, 385  
 Garilli B., et al., 2008, *A&A*, 486, 683  
 Glazebrook K., Blake C., 2005, *ApJ*, 631, 1  
 Glazebrook K., et al., 2007, *ASPC*, 379, 72  
 Hambly N. C., et al., 2001, *MNRAS*, 326, 1279  
 Hütsi G., 2006, *A&A*, 449, 891  
 Hu W., Haiman Z., 2003, *PhRvD*, 68, 063004  
 Ilbert O., et al., 2006, *A&A*, 457, 841  
 Ivezić Ž., et al., 2004, *AN*, 325, 583  
 Jones D. H., et al. 2004, *MNRAS*, 355, 747  
 Kewley L. J., Dopita M. A., Sutherland R. S., Heisler C. A., Trevena J., 2001, *ApJ*, 556, 121  
 Kinney A. L., Calzetti D., Bohlin R. C., McQuade K., Storchi-Bergmann T., Schmitt H. R., 1996, *ApJ*, 467, 38  
 Komatsu E., et al., 2009, *ApJS*, 180, 330  
 Linder E. V., 2003, *PhRvD*, 68, 083504  
 Martin D. C., et al., 2005, *ApJ*, 619, L1  
 Metropolis N., Rosenbluth A. W., Rosenbluth M. N., Teller A. H., Teller E., 1953, *J. Chem. Phys.*, 21  
 Miszalski, B. et al. 2006, *MNRAS*, 371, 1537.  
 Monet D. G., et al., 2003, *AJ*, 125, 984  
 Morrissey P., et al., 2007, *ApJS*, 173, 682  
 Ostriker J. P., Steinhardt P. J., 1995, *Natur*, 377, 600  
 Parkinson D., Blake C., Kunz M., Bassett B. A., Nichol R. C., Glazebrook K., 2007, *MNRAS*, 377, 185  
 Percival W. J., Cole S., Eisenstein D. J., Nichol R. C., Peacock J. A., Pope A. C., Szalay A. S., 2007, *MNRAS*, 381, 1053  
 Perlmutter S., et al., 1999, *ApJ*, 517, 565  
 Riess A. G., et al., 1998, *AJ*, 116, 1009  
 Riess A. G., et al., 2007, *ApJ*, 659, 98  
 Saunders W., et al., 2004, *SPIE*, 5492, 389  
 Scherrer R. J., Weinberg D. H., 1998, *ApJ*, 504, 607  
 Schlegel D. J., Finkbeiner D. P., Davis M., 1998, *ApJ*, 500, 525 (SFD)  
 Schlegel D., White M., Eisenstein D., 2009, [arXiv:0902.4680v1](http://arxiv.org/abs/0902.4680v1)  
 Seo H.-J., Eisenstein D. J., 2003, *ApJ*, 598, 720  
 Seo H.-J., Eisenstein D. J., 2007, *ApJ*, 665, 14  
 Sharp R., et al., 2006, *SPIE*, 6269, 62690G

- Shortridge K., Ramage C., Farrell T., 2006,  
“2dF/6dF/AAOmega CONFIGURE User Manual v.1.5”,  
see <http://www.aao.gov.au/AAO/2df/aaomega/>
- Skrutskie M. F., et al., 2006, *AJ*, 131, 1163
- Smith G. A., et al., 2004, *SPIE*, 5492, 410
- Steidel C. C., Giavalisco M., Dickinson M., Adelberger  
K. L., 1996, *AJ*, 112, 352
- Tonry J., Davis M., 1979, *AJ*, 84, 1511
- Wild V., Hewett P. C., 2005, *MNRAS*, 358, 1083
- Wood-Vasey W. M., et al., 2007, *ApJ*, 666, 694
- Wyder T. K., et al., 2007, *ApJS*, 173, 293
- Yee H. K. C., Gladders M. D., Gilbank D. G., Majumdar  
S., Hoekstra H., Ellingson E., 2007, *ASPC*, 379, 103
- York D. G., et al., 2000, *AJ*, 120, 1579
- Yoshii Y., Peterson B. A., 1995, *ApJ*, 444, 15
- Yoshii Y., Peterson B. A., 1991, *ApJ*, 372, 8

This paper has been typeset from a  $\text{\TeX}/\text{\LaTeX}$  file prepared  
by the author.